

# 1 Impact of Internal Tides on Chlorophyll-a Distribution and Primary 2 Production off the Amazon Shelf from Glider Measurements and 3 Satellite Observations

4 Amine M'hamdi<sup>1,2,8</sup>, Ariane Koch-Larrouy<sup>1,8</sup>, Alex Costa da Silva<sup>2</sup>, Isabelle Dadou<sup>1</sup>, Carina Regina de  
5 Macedo<sup>1,3,7</sup>, Anthony Bosse<sup>12</sup>, Vincent Vantrepotte<sup>3,2</sup>, Habib Micaël Aguedjou<sup>1,11</sup>, Trung-Kien Tran<sup>3</sup>,  
6 Pierre Testor<sup>9</sup>, Laurent Mortier<sup>10</sup>, Arnaud Bertrand<sup>4</sup>, Pedro Augusto Mendes de Castro Melo<sup>2</sup>, James  
7 Lee<sup>5</sup>, Marcelo Rollnic<sup>5</sup>, Moacyr Araujo<sup>2,6</sup>

8 <sup>1</sup>LEGOS, Université de Toulouse, CNRS, OMP, IRD, Toulouse, France.

9 <sup>2</sup>Departamento de Oceanografia, Universidade Federal de Pernambuco (DOCEAN/UFPE), Recife, Brazil.

10 <sup>3</sup>Univ. Littoral Côte d'Opale, CNRS, Univ. Lille, IRD, UMR 8187 - LOG - Laboratoire d'Océanologie et de Géosciences, F-  
11 62930 Wimereux, France.

12 <sup>4</sup>MARBEC, Université de Montpellier, CNRS, Ifremer, IRD, Sète, France.

13 <sup>5</sup>Departamento de Oceanografia, Universidade Federal do Pará (UFPA), Belém, Brazil.

14 <sup>6</sup>Brazilian Research Network on Global Climate Change (Rede CLIMA), 12227-010, São José dos Campos-SP, Brazil.

15 <sup>7</sup>Earth Observation and Geoinformatics Division, National Institute for Space Research (INPE), São José dos Campos,  
16 Brazil.

17 <sup>8</sup>CECI CNRS/Cerfa/IRD, Université de Toulouse, Toulouse, France.

18 <sup>9</sup>LOCEAN-IPSL/CNRS, Université Pierre et Marie Curie, 745-55 E4 case 100, 4 place Jussieu 75252 Paris, France.

19 <sup>10</sup>École Nationale Supérieure de Techniques Avancées, 29 rue d'Ulm, F-75230 Paris cedex 05, France.

20 <sup>11</sup>Centre National d'Études Spatiales, 18 av. Edouard Belin 31400 Toulouse, France.

21 <sup>12</sup>Mediterranean Institute of Oceanography, OSU Institut Pytheas, Aix Marseille University, Université de Toulon, CNRS,  
22 IRD, Marseille, France.

23 Correspondence to: Amine M'hamdi (abn.mhamdi@gmail.com)

## 24 Abstract.

25 The ocean region off the Amazon shelf including shelf-break presents a hotspot for Internal Tides (ITs) generation, yet its  
26 impact on phytoplankton distribution remains poorly understood. ~~These baroclinic waves, generated by tidal interactions with~~  
27 ~~topography, could modulate nutrient availability and primary production both by mixing and advection.~~ While previous studies  
28 have extensively examined the physical characteristics and dynamics of ITs, their biological implications—particularly in  
29 nutrient-limited environments—remain underexplored. To address this question, we analysed a 26-day glider mission deployed  
30 in September–October 2021 sampling hydrographic and optical properties (chlorophyll-a) at high resolution along an IT  
31 pathway, satellite chlorophyll-a and altimetry data to assess mesoscale interactions. Chlorophyll-a dynamics were analysed  
32 under varying IT intensities, comparing strong (HT) and weak (LT) internal tide conditions. Results reveal that ITs drive  
33 vertical displacements of the Deep chlorophyll Maximum (DCM) from 15 to 45 meters, accompanied by ~~a remarkable~~ 50%  
34 expansion in its thickness during HT events. This expansion is observed with a dilution of the chlorophyll-a maximum

a mis en forme: En-tête

Définition du style: Titre 1

Définition du style: Titre 2

Définition du style: Titre 3

Définition du style: Titre 4

Définition du style: Titre 5

Définition du style: Titre 6

Définition du style: Police par défaut

Définition du style: Titre

Définition du style: Sous-titre

a mis en forme: Police :+Titres CS (TimesNew Roman)

a mis en forme: Police :+Titres CS (TimesNew Roman), Français (France)

a mis en forme: Police :+Titres CS (TimesNew Roman)

a mis en forme: Police :+Titres CS (TimesNew Roman), Français (France)

a mis en forme: Police :+Titres CS (TimesNew Roman)

a mis en forme: Police :+Titres CS (TimesNew Roman), Français (France)

a mis en forme: Police :+Titres CS (TimesNew Roman)

a mis en forme: Police :+Titres CS (TimesNew Roman)

a mis en forme: Police :+Titres CS (TimesNew Roman)

35 concentration within the DCM depth. ~~Turbulent~~ While direct turbulence measurements were not collected, the observed  
 36 vertical redistribution of chlorophyll-a is indicative of tidally driven cross-isopycnal exchanges driven by tides redistribute  
 37 chlorophyll-a into adjacent layers, the only physical mechanism to explain the transfer of biomass above and below the DCM.  
 38 At the surface, turbulent fluxes contribute to provide 38% of the chlorophyll-a supply, which directly influences primary  
 39 production input, while the remainder is supplied by in situ biological activity. Notably, the total chlorophyll-a content in the  
 40 water column increases by 14–29% during high internal tide phases, reflecting indicating a net enhancement of primary  
 41 productivity. This increase results from driven by the combined effects of vertical mixing and stimulated biological  
 42 activity in the surface-layer biological activity. These findings highlight the role of ITs as a key indicate that internal tides can  
 43 be an important driver of chlorophyll-a distribution and short-term biological variability in our study region. By reshaping the  
 44 vertical chlorophyll-a profile and regulating through vertical mixing, active internal tides influence primary productivity and  
 45 potentially may contribute to carbon cycling, particularly in oligotrophic oceanic systems environments where both a deep  
 46 chlorophyll maximum and strong internal tides are present.

## 47 1 Introduction

48 Internal Tides (ITs), also known as baroclinic tides, are ubiquitous in stratified oceans. These waves cause vertical  
 49 displacements of isopycnal layers on the order of tens of meters and can propagate over long distances, reaching up to  
 50 thousands of kilometers along the thermocline for the lowest modes (Zhao et al., 2016). Baroclinic tides are generated through  
 51 the interaction of barotropic tidal currents with prominent submarine topographies such as continental slopes and mid-ocean  
 52 ridges (Baines, 1982; Egbert and Ray, 2001; Munk and Wunsch, 1998). Internal solitary waves (ISWs) are highly stable  
 53 internal waveforms that can propagate over long distances with a crest of a few tens of kilometers, and are generally structured  
 54 with a wave train trailing behind the main crest (Alford et al., 2015; Jackson et al., 2012; Jeans and Sherwin, 2001). In addition  
 55 to ITs, shorter wavelength internal solitary waves (ISWs) may form from the nonlinear properties of ITs and dispersive  
 56 processes, accompanying the ITs (Grimshaw, 2003; Grisouard et al., 2011). During their propagation, ITs and ISWs may  
 57 eventually break down, releasing energy and driving vertical turbulent mixing (Alford et al., 2015; Lamb and Xiao, 2014;  
 58 Meum et al., 2003; Nash et al., 2004). The generation mechanisms and evolution of ISWs have attracted considerable attention in recent  
 59 decades (Bai et al., 2021; Buijsman et al., 2010; Raju et al., 2021; Yuan et al., 2023). Their occurrence often serves as a direct indicator of  
 60 the presence and nonlinear evolution of internal tides. ISWs are most commonly formed through the nonlinear transformation of  
 61 internal tides (ITs) as they evolve (Farmer et al., 2009; Zhang et al., 2011). More recently, river plumes have been identified  
 62 as a source of ISWs in stratified coastal regions, where the density fronts generated by freshwater outflows can trigger wave  
 63 generation. Examples include the Douro River plume off the Portuguese coast (Mendes et al., 2021), the Rhine River plume  
 64 in the southern North Sea (Rijnsburger et al., 2021), and the Mzymta River plume in the Black Sea (Osadchiev, 2018). As they  
 65 propagate, internal tides (ITs) and, to a lesser extent, internal solitary waves (ISWs) can break, releasing energy and inducing  
 66 vertical turbulent mixing, with ITs often representing the dominant source of such mixing in stratified coastal and shelf seas

67 [\(Alford et al., 2015; Lamb and Xiao, 2014; Moum et al., 2003; Nash et al., 2004\)](#). This mixing can play a crucial role in general  
68 circulation, contributing to the enclosure of the Atlantic Meridional Overturning Circulation (AMOC), and influencing oceanic  
69 energy and heat fluxes (Kantha and Tierney, 1997; Kunze, 2017; Waterhouse et al., 2014). Furthermore, [because](#) this mixing  
70 occurs close to the surface, [it may also](#) influence climate variability (Koch-Larrouy et al., 2010; Sprintall et al.,  
71 2014) through air-sea interactions. By altering sea surface temperature, it can modulate atmospheric convection, humidity,  
72 and precipitation patterns, as observed in the Indonesian seas where IT-induced mixing leads to surface cooling and reduced  
73 rainfall (Koch-Larrouy et al., 2010; Sprintall et al., 2014).

74 While the physical characteristics of ITs have been extensively studied, their impact on biogeochemical processes remains  
75 relatively poorly explored (Holligan et al., 1985; Liu et al., 2006; Ma et al., 2023; Zaron et al., 2023). Their influence on  
76 plankton dynamics is of significant interest, as phytoplankton constitutes the lowest trophic level of marine ecosystems.  
77 Through photosynthesis and organic carbon production, phytoplankton regulates primary productivity and influences global  
78 biogeochemical cycles (Falkowski and Knoll, 2007). The spatial and temporal variability of phytoplankton populations is  
79 driven by a combination of biological factors, such as production and grazing, and physical processes, including ocean currents,  
80 mesoscale structures (fronts and eddies), and heat fluxes (Mahadevan and Campbell, 2002; Van Gennip et al., 2016). Given  
81 the timescale and amplitude of disturbances generated by ITs, it is reasonable to hypothesize that ITs can significantly influence  
82 phytoplankton distribution.

83 The effects of ITs on phytoplankton could occur through, at least, two primary mechanisms. First, vertical mixing induced by  
84 ITs can enhance nutrient fluxes into the euphotic zone, stimulating primary production and increasing phytoplankton biomass  
85 in regions with high IT activity (Bourgault et al., 2011; Capuano et al., 2025; Horne et al., 1996; Kaneko et al., 2025; Law et  
86 al., 2003; Lewis et al., 1986; Martin et al., 2010; Tsutsumi et al., 2020; Tuerena et al., 2019; Zaron et al., 2023). Second, the  
87 vertical displacements associated with ITs can alter the light and nutrient conditions experienced by phytoplankton cells near  
88 the pycnocline, thereby influencing their physiological responses and community structure (Gaxiola-Castro et al., 2002;  
89 Holloway and Denman, 1989; Jacobsen et al., 2023; Kahru, 1983; Lande and Yentsch, 1988; Sangrà et al., 2002; Vázquez et  
90 al., 2009).

91 The Amazon shelf-break is recognized as a hotspot for internal tide (IT) generation, dissipation and interact with intense  
92 mesoscale features. First identified by Baines, 1982, subsequent studies have confirmed its role in converting barotropic energy  
93 into baroclinic waves (Assene et al., 2024; Brandt et al., 2002; De Macedo et al., 2023; Ivanov et al., 1990; Magalhaes et al.,  
94 2016; Tchilibou et al., 2022; Vlasenko et al., 2005). However, the specific impacts of these ITs on biological processes off  
95 Amazon, particularly phytoplankton dynamics in the region, remain poorly understood and require further investigation.

96 This region, [\(Fig. 1\)](#), situated in the western tropical Atlantic near the mouth of the Amazon and Pará rivers, features a shallow  
97 continental shelf and a macrotidal regime predominantly influenced by the semi-diurnal M2 tidal component (Beardsley et al.,

a mis en forme : En-tête

a mis en forme : Police :+Titres CS (TimesNew Roman), Anglais (États-Unis)

a mis en forme : Police :+Titres CS (TimesNew Roman)

a mis en forme : Police :+Titres CS (TimesNew Roman)

a mis en forme : Police :+Titres CS (TimesNew Roman)

a mis en forme : Police :+Titres CS (TimesNew Roman), 9 pt, Anglais (États-Unis)

a mis en forme : Police :+Titres CS (TimesNew Roman), 9 pt, Français (France)

a mis en forme : Police :+Titres CS (TimesNew Roman)

98 1995; Gabiou et al., 2005). The Amazon River significantly shapes local oceanographic conditions by modifying salinity,  
99 temperature, and water column stratification (Geyer, 1995; Ruault et al., 2020). During the August-September-October (ASO)  
100 season, reduced river discharge leads to a weaker and deeper pycnocline, along with a stronger North Brazil Current (NBC)  
101 and higher eddy kinetic energy (EKE) (Neto and Da Silva, 2014; Silva et al., 2005; Tchilibou et al., 2022). The isopycnal  
102 layers are thicker nearshore and become tighter offshore, causing weaker coastal stratification that increases offshore. These  
103 seasonal variations clearly highlight the dynamic shifts in vertical density gradients, consistent with observations by Aguedjou  
104 et al., 2019, [making the ASO season one of the optimal periods for investigating internal tides in the region.](#)

105

106 The dynamics of this region are further shaped by interactions with the NBC, a major western boundary current transporting  
107 warm, saline waters from the South Atlantic (Garzoli et al., 2003; Johns et al., 1998; Schott et al., 1998; Silva et al., 2005).  
108 Between June and February, the NBC undergoes a seasonal retroflection, forming large anticyclonic rings that propagate  
109 northwestward (Fratantoni and Richardson, 2006; Fratantoni and Glickson, 2002). These anticyclonic eddies, known as “NBC  
110 rings”, can modulate stratification and nutrient distributions, influencing phytoplankton productivity (Mikaelyan et al., 2020).  
111 During the second part of the year a large part of the NBC retroflects to feeds the eastward North Equatorial Countercurrent  
112 (NECC) (Dimoune et al., 2023).

113 To investigate the role of ITs in shaping phytoplankton dynamics in the oceanic region off the Amazon shelf, the AMAZOMIX  
114 cruise aimed to collect a wide range of in situ measurements. Conducted between September and October 2021—an optimal  
115 period for IT activity and mesoscale interactions—the cruise employs a multi-faceted approach combining numerical models,  
116 satellite data, and in situ observations. In addition to ship-based measurements, an autonomous underwater glider was deployed  
117 from September 9 to October 5, 2021 to have high resolution vertical structure data (hydrographic and chlorophyll-a)  
118 influenced by ITs.

119 The objective of this study is to investigate how ITs influence the vertical distribution of Chlorophyll-a concentration off the  
120 Amazon shelf. Analyses were performed by examining glider measurements and remote sensing observations, and by  
121 comparing periods of strong and weak internal tide activity under similar stratification conditions.

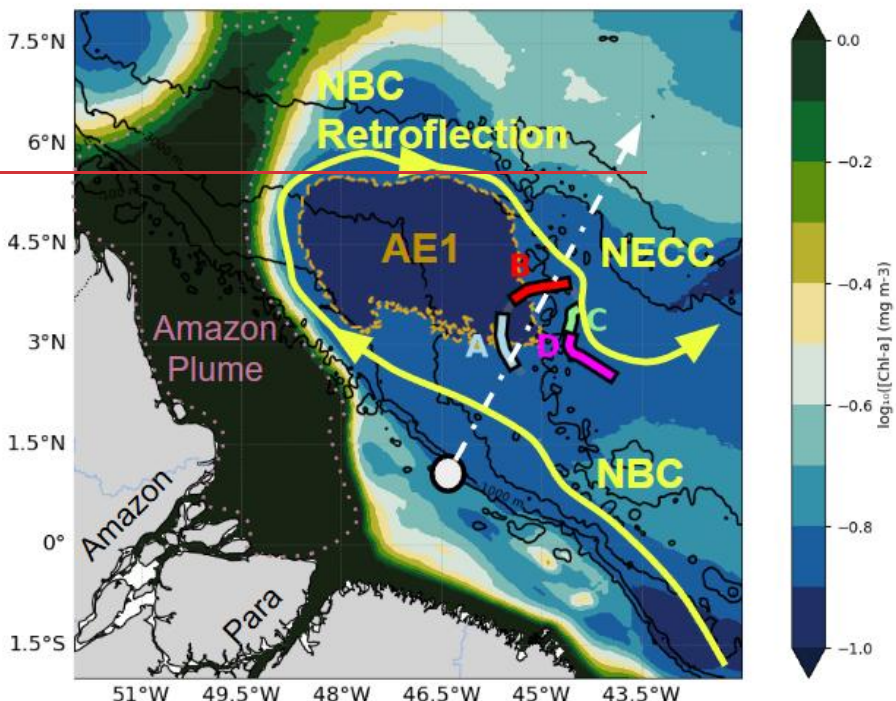
122 **2 Data and Methods**123 **2.1 Data**124 **2.1.1 Autonomous glider**

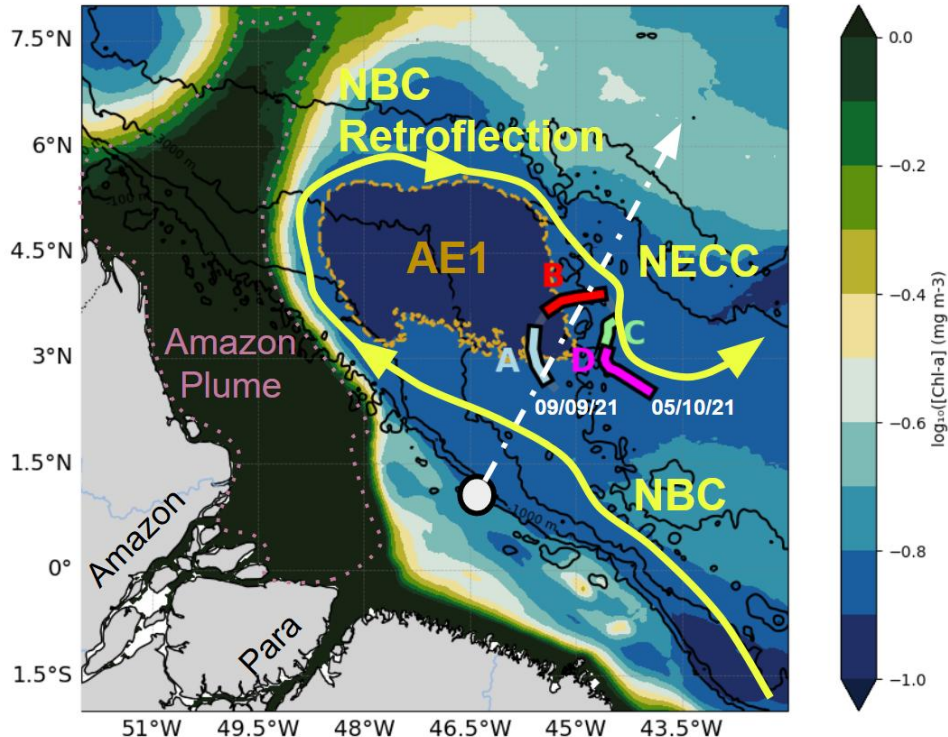
125 On September 9, 2021, during the AMAZOMIX campaign an autonomous underwater glider (Testor et al., 2019)  
 126 was deployed for 26 days (09/09-05/10/ 2021) between the NBC and NECC, the adjacent oceanic waters off the  
 127 Northern Brazil (Figure 1) in the core of an ITs propagation path identified by Magalhaes et al., 2016 and Tchilibou  
 128 et al., 2022 . A Slocum G2 glider from Teledyne Webb Research was used, which is able to dive to 1000 m within  
 129 four hours and to cover approximately 20 km horizontally per day relative to the water, which can reach 1000 m  
 130 in four hours and cover about 20 km per day relative to the water, assuming optimal conditions and no currents.

131 Due to strong currents near 1 m/s representing a real challenge for glider operation, the glider only completes a  
 132 total distance of 315 km over ground during the 26-day deployment. The glider was equipped with a Seabird's  
 133 pumped CTD (temperature, pressure, conductivity), an Aanderaa optode (dissolved oxygen), and a WetLabs's  
 134 optical puck (chlorophyll-a fluorescence, CDOM, and turbidity). The sensors had a sampling frequency of 5  
 135 seconds, resulting in a vertical sampling interval of approximately 1 m. Between each surfacing, the glider estimates  
 136 its position thanks to using navigation sensors (compass) enabling to estimate allowing estimation of a mean dive-  
 137 average horizontal currents while comparing its dead-reckoned position with GPS fixes. The glider dataset was  
 138 processed using the Geomar Matlab Toolbox (Krahmann, 2023), which includes the removal of thermal lag errors  
 139 following (Garau et al., 2011). All scientific and system data were linearly interpolated to 1-second intervals,  
 140 aligning science and navigation variables with the glider's main processor clock. The interpolation introduces  
 141 minimal additional noise, as the vertical displacement of the glider over one second is typically <0.2 m. In the  
 142 vertical, data from each dive profile (yo) were binned and averaged into 1 dbar intervals, and then interpolated  
 143 linearly to produce uniformly gridded vertical profiles. These profiles were used in all subsequent analyses,  
 144 including spectral decomposition, stratification diagnostics, and vertical chlorophyll characterization. After the  
 145 standard GEOMAR gridding (1 dbar vertically and timestamp alignment), we applied a second linear interpolation  
 146 in time to project the variables onto a common regular temporal grid. This interpolation was performed  
 147 independently at each depth level using valid (non-NaN) observations, ensuring a complete and consistent 2D  
 148 structure across depth and time. These interpolated matrices were used for spectral and variability analyses

149 Temperature and salinity were converted to conservative temperature and absolute salinity using the Gibbs  
 150 Seawater python library (McDougall and Barker, 2011). The temperature and salinity profiles were validated by

151 comparison with a reference CTD at the glider deployment site. Daytime chlorophyll-a fluorescence profiles were  
152 corrected for non-photochemical quenching processes using the method described by (Thomalla et al., 2018),  
153 setting the quenching depth at 40 m. To enable direct comparison with satellite-derived data, chlorophyll-a  
154 concentrations measured by the glider were averaged from the surface down to the first optical depth ( $Z_{pd} = Zeu/4.6$   
155 Morel, 1988) to build the time series, which defines the depth range primarily sensed by ocean colour remote  
156 sensors.





158  
159 **Figure 1 :** Chlorophyll map averaged between 09/09/21 and 05/10/21 in the glider deployment region, divided into four subregions:  
160 A (blue), B (red), C (green), and D (magenta), each characterized by distinct temperature-salinity (T/S) properties (section 3.1). The  
161 yellow area marks the main surface current, purple indicates the plume, and light brown highlights AE1, the anticyclonic eddy  
162 detected by altimetry during the transect. The white dashed line shows the main internal tide propagation pathways identified by  
163 Magalhães et al. (2016) and Tchilibou et al. (2022), while the grey circle marks the primary internal tide generation site ( $46^{\circ}$  /  $0.75^{\circ}$ ).

164 **2.1.2 Remote sensing observations: ISW detection, Chlorophyll-a distribution and Mesoscale eddy tracking**

165 Internal solitary waves (ISWs) create patterns alternating between rough and smooth surface areas, corresponding to  
166 convergent and divergent surface currents, respectively. Thus, their signatures in MODIS images during sunglint or in the SAR  
167 imagery are manifested by variations in sea surface roughness, resulting in changes in the brightness of the captured images (De

168 Macedo et al., 2023; Jackson and Alpers, 2010; Magalhaes et al., 2016). During the cruise, ISW signatures were visually  
169 identified and manually extracted off the Amazon shelf from a representative assembled data set composed of 21 remote  
170 sensing imagery acquired by active and passive sensors from 1st September 2021 to 10th October 2021. A total of 13  
171 ~~imagery~~images were acquired by the synthetic aperture radar (SAR) C-band (centre frequency of 5.4 GHz) Copernicus  
172 Sentinel-1A and 1B instruments Level-1 GRD (ground range detected) products in the interferometric wide swath mode with  
173 about 250 km of swath and spatial resolution of 20.3 x 22.6 m (range x azimuth), operating in single polarization (VV channel).  
174 The SAR imagery were collected from the Copernicus Open Access Hub (<https://scihub.copernicus.eu/dhus/#/home>). The  
175 SAR scenes were pre-processed using the software SNAP and Sentinel Toolboxes (version 8.0) by calibrating the data  
176 (conversion from digital number to normalised radar cross-section) and applying a 5x5 boxcar filter to reduce the speckle  
177 noise. A total of 8 Level 1B imagery were acquired by the Moderate Resolution Imaging Spectroradiometer (MODIS) sensor  
178 onboard the TERRA and AQUA satellites. The band 6 centred at 1640 nm with a spatial resolution of 500 m was used to  
179 identify the ISW signatures in the sun glint region. The MODIS/TERRA and AQUA imagery were collected from NASA's  
180 Earth Science Data System, ESDS (<https://earthdata.nasa.gov/>).

181

182 Given that ocean colour observations are often affected by interference from clouds, leading to data gaps, we used the daily  
183 mean merged chlorophyll-a (with a spatial resolution of ~4 km) product from the GlobColour project to maximise data  
184 coverage from 1st September 2021 to ~~05-th-05th~~ October 2021 provided by the ACRI-ST company (Garnesson et al., 2019).  
185 This product provides chlorophyll-a concentration information from the ocean colour sensors MODIS-AQUA, NPP-VIIRS,  
186 NOAA20-VIIRS, and Sentinel-3 OLCI A and B, including updated ancillary information (i. e., meteorological and ozone data  
187 for atmospheric correction, and attitude and ephemerides for data geolocation). According to Garnesson et al., 2019, the  
188 approach ~~merges~~merges three algorithms: 1) the CI approach for oligotrophic waters (Hu et al., 2012) ; 2) the OCx (OC3, OC4  
189 or OC4Me depending on the sensor) for mesotrophic waters; and 3) the OC5 algorithm for complex waters (Gohin, 2011). The  
190 product can be found on the CMEMS website (<https://resources.marine.copernicus.eu/products>). In this study, we utilized data  
191 provided by GlobColour, specifically estimates of the euphotic depth (Zeu) derived from satellite observations of the MODIS-  
192 Aqua sensor. These Level-3 processed data are available at a spatial resolution of 4 km and were obtained from the GlobColour  
193 platform. The euphotic depth was estimated following the methodology described by Morel and Maritorena (2001), which ~~is~~  
194 based on an empirical relationship linking surface chlorophyll-a concentration to light penetration depth, which defines Zeu as  
195 the depth where incident light is reduced to 1% of its surface value. The dataset is publicly available at HERMES ACRI.

196

197 Daily maps of the Ssalto/Duacs absolute dynamic topography (ADT) gridded product were used to identify and track coherent  
198 mesoscale eddies during AMAZOMIX campaign. This product was obtained from all available satellite altimetry along-track  
199 data and optimally interpolated onto a 0.25°x0.25° longitude/latitude (Pujol et al., 2016).~~The product can be found on :~~  
200 [https://data.marine.copernicus.eu/product/SEALEVEL\\_GLO\\_PHY\\_MDT\\_008\\_063/description](https://data.marine.copernicus.eu/product/SEALEVEL_GLO_PHY_MDT_008_063/description)

a mis en forme : En-tête

a mis en forme : Police :+Titres CS (TimesNew Roman)

201 Mesoscale eddies were identified, using the algorithm developed by Chaigneau et al., 2009, 2008; Pegliasco et al., 2015. In  
202 this method, an eddy is identified by its centre and its external edge. An eddy centre corresponds to a local extremum  
203 (maximum for an anticyclonic eddy and minimum for a cyclonic eddy) in ADT while eddy edge corresponds to the outermost  
204 closed ADT contour around each detected eddy centre. One long-lived anticyclonic eddy (AE1) was identified during the  
205 AMAZOMIX campaign. AE1 was generated within the study domain from instability of NECC and propagated north  
206 westward making NECC oscillating the NBC figure 3 . AE1 lasted more than 120 days. The bathymetric data used in this  
207 study are sourced from the NOAA CoastWatch Program and are accessible through the NOAA CoastWatch Data Portal. These  
208 data are formatted for MATLAB and are stored under the directory gov.noaa.pfel.coastwatch.Matlab. The bathymetric dataset,  
209 referenced from the Topography SRTM30 Version 6.0 (30 Arc-Second Global), provides detailed seafloor topography  
210 information crucial for analysing oceanographic processes. Additionally, the geostrophic velocity data used in this study are  
211 sourced from the Global Ocean Gridded SSALTO/DUACS Sea Surface Height L4 product, provided by Mercator through the  
212 Copernicus Marine Service. This product includes surface geostrophic eastward and northward sea water velocities, calculated  
213 from sea surface height assuming sea level as the geoid reference. These data, derived from sea surface height, provide essential  
214 surface currents. The dataset is available via Copernicus Marine Data .

### 215 2.1.3 FES model

216 Tidal data were extracted from the global FES2014 (Finite Element Solution) model developed by Lyard et al., 2021. The  
217 outputs of the sea surface elevation field (eta) were used at the grid point corresponding to 46°N, 0.75°E, which corresponds  
218 to an internal tide generation site previously identified by Magalhaes et al., 2016 and Tchilibou et al., 2022. The use of those  
219 data helped us to identify neap tides and spring tides.

### 220 2.2 Methods

221 To assess the impact of ITs (ITs) on the vertical distribution of chlorophyll-a (hereafter referred as CHL for the equations), a  
222 multi-step approach was applied. (1) Satellite observations were used to characterize the large-scale spatial distribution of  
223 chlorophyll-a and the physical processes influencing it, enabling the identification of hydrographically distinct regions (section  
224 3.1) (2) Based on this preliminary analysis, the glider data were divided into transects corresponding to representing four  
225 periods (A, B, C, and D; Fig. 1; Section 3.2) with contrasting hydrographic properties named A, B, C and D (Fig. 1) (Section  
226 3.2). These periods were defined from marked changes in temperature, salinity, and potential density structure, identified  
227 through visual inspection of vertical profiles and T-S diagrams, focusing on shifts in stratification patterns and salinity ranges  
228 across isopycnal layers. (3) Given the prevalence of ITs in the study area, A and B period was further subdivided into low tide  
229 (LT) and high tide (HT) phases using spectral analysis of the temperature field to estimate tidal amplitude; the classification  
230 was based on the presence of a spectral peak at the M2 frequency (section 3.2). (4) Chlorophyll-a fluorescence profiles  
231 collected by the glider were then averaged and statistically compared between LT and HT conditions to evaluate the effect of

a mis en forme : Police :+Titres CS (TimesNew Roman)

a mis en forme : Police :+Titres CS (TimesNew Roman)

a mis en forme : Police :+Titres CS (TimesNew Roman)

a mis en forme : Police :+Titres CS (TimesNew Roman)

a mis en forme : Police :+Titres CS (TimesNew Roman)

232 IT intensity on chlorophyll-a vertical distribution (section 3.3). (5) Finally, vertical turbulent fluxes of chlorophyll-a were  
 233 estimated to better understand the transport mechanisms associated with ITs (section 3.3 ).

### 234 2.2.1 Temperature Power Spectra

235 We analysed temperature time series between ~~145m~~<sup>145 m</sup> and 165 m depth, where the largest vertical displacement of  
 236 isotherms was observed. The high-frequency glider profiling (about 12 profiles per day) enabled the construction of  
 237 temperature time series resolving the main tidal frequency (42h) ~~All~~<sup>12</sup> h). To compute the power spectra of temperature  
 238 variability at this depth interval, all measurements between within the ~~145 and 165 meters~~<sup>m</sup> range were aggregated treated  
 239 equally, without vertical weighting, and concatenated into a single composite 1D time series. The resulting signal, sampled at  
 240 irregular intervals due to glider motion, was interpolated onto a uniform time grid using  
 241 `pandas.resample('1H').mean().interpolate()`, which performs hourly averaging followed by linear interpolation over missing  
 242 values. This procedure ensures temporal regularity and allows consistent application of Fourier analysis. While no formal  
 243 vertical averaging was applied, the method assumes that variability within the selected layer is coherent enough to be  
 244 represented by a single aggregated signal. Prior to computing the spectra, a Hanning window was applied to the time series to  
 245 reduce spectral leakage, zero-padding was used to increase frequency resolution, and a 10-point moving average was applied  
 246 to the resulting power spectrum for clearer visualization. The aggregated time series was resampled at 30 mins to ensure  
 247 regularly spaced data points and then detrended to remove long-term variations. A Fast Fourier Transform (FFT) was  
 248 then applied to convert the time series into the frequency domain. The power spectrum was calculated to identify the dominant  
 249 oscillation frequencies of oscillations (McInemey et al., 2019) (McInemey et al., 2019).

### 250 2.2.2 Diapycnal chlorophyll fluxes estimation

251 The vertical dynamics of chlorophyll-a concentration (CHL) in the water column is described by the following  
 252 equation :

253 The vertical dynamics of chlorophyll-a concentration (CHL) in the water column is described by the following  
 254 equation adapted from the vertically resolved NPZ formulation (Franks, 2002), with the physical transport term representing  
 255 cross-isopycnal turbulent fluxes associated with internal tides. :

$$256 \frac{\partial CHL(z,t)}{\partial t} + w \frac{\partial}{\partial z} CHL(z,t) = \frac{\partial}{\partial z} (Kz \frac{\partial}{\partial z} CHL(z,t)) + SMS(z,t) \quad (1)$$

257 Where CHL is the chlorophyll-a concentration. The  $w \frac{\partial}{\partial z} CHL(z,t)$  term represents the vertical advection of chlorophyll by  
 258 the vertical velocity field w, while  $\frac{\partial}{\partial z} (Kz \frac{\partial}{\partial z} CHL(z,t))$  accounts for vertical turbulent diffusion, with Kz being the diffusivity

a mis en forme : Police :+Titres CS (TimesNew Roman)

a mis en forme : Police :+Titres CS (TimesNew Roman)

a mis en forme : Police :+Titres CS (TimesNew Roman)

a mis en forme : Police :+Titres CS (TimesNew Roman)

a mis en forme : Police :+Titres CS (TimesNew Roman)

a mis en forme : Police :+Titres CS (TimesNew Roman)

a mis en forme : Police :+Titres CS (TimesNew Roman)

a mis en forme : Police :+Titres CS (TimesNew Roman)

a mis en forme : Police :+Titres CS (TimesNew Roman)

a mis en forme : Police :+Titres CS (TimesNew Roman)

a mis en forme : Police :+Titres CS (TimesNew Roman)

a mis en forme : Police :+Titres CS (TimesNew Roman)

a mis en forme : Police :+Titres CS (TimesNew Roman)

a mis en forme : Police :+Titres CS (TimesNew Roman)

a mis en forme : Police :+Titres CS (TimesNew Roman), Anglais (États-Unis)

a mis en forme : Police :+Titres CS (TimesNew Roman)

a mis en forme : Police :+Titres CS (TimesNew Roman)

a mis en forme : Police :+Titres CS (TimesNew Roman)

a mis en forme : Police :+Titres CS (TimesNew Roman)

a mis en forme : Police :+Titres CS (TimesNew Roman)

a mis en forme: En-tête

259 coefficient. The source-minus-sink (SMS) term encompasses biological processes, specifically primary production and  
260 grazing, which regulate the net chlorophyll-a balance in the system.

261 To isolate turbulent chlorophyll-a fluxes, the analysis is conducted within a vertical isopycnal reference framework. In this  
262 context, the advection term  $w \frac{\partial}{\partial z} CHL(z) = 0$  as vertical velocities advect isopycnals up and down. By changing the vertical  
263 coordinate from  $z$  to rho  $\frac{\partial CHL(\rho(z))}{\partial z} = \frac{\partial \rho}{\partial z} \frac{\partial CHL(\rho(z))}{\partial \rho}$  and assuming  $\frac{\partial \rho}{\partial z}$  and  $K_z$  is constant leads to the equation:

$$\frac{\partial CHL(\rho, t)}{\partial t} = K_v \frac{\partial^2 CHL(\rho, t)}{\partial \rho^2} + SMS(\rho) \quad (2)$$

264 Where the constant  $K_v = \left(\frac{\partial \rho}{\partial z}\right)^2 K_z = \left(\frac{N^2 \rho_0}{g}\right)^2 K_z$  represents the diapycnal diffusivity coefficient with  $\rho_0$  the mean density of  
265 the ocean and  $g$  the gravitational acceleration. By integrating between two isopycnal density surfaces ( $\rho_0$  and  $\rho_1$ ), the average  
266 variations over a given period ( $\Delta T$ ) are defined as:

$$\langle P \rangle_{\rho_0, \rho_1, \Delta T} = \frac{1}{\Delta T} \int_{\rho_0}^{\rho_1} \int \frac{\partial P(\rho, t)}{\partial t} d\rho dt \quad (3)$$

$$\langle P \rangle_{\rho_0, \rho_1, \Delta T} = \frac{1}{\Delta T} \int_{\rho_0}^{\rho_1} \int \frac{\partial P(\rho, t)}{\partial t} d\rho dt \quad (3)$$

267 Where  $P$  correspond either to  $\frac{\partial CHL(\rho, t)}{\partial t}$ ;  $K_v \frac{\partial^2 CHL(\rho, t)}{\partial \rho^2}$ ;  $SMS(\rho)$  and  $\langle P \rangle$  to  $\langle CHL \rangle$ ,  $\langle DIFF \rangle$  or  $\langle SMS \rangle$

271 For two distinct periods corresponding to complete tidal cycles with intense tides  $\Delta HT$  and low tides  $\Delta LT$ , and within a  
272 density layer between  $\rho_0$  and  $\rho_1$ , the differences are defined as: High Tidal Forcing (HT) and Low Tidal Forcing (LT) were  
273 defined within each observation window based on the relative intensity of internal tide activity. HT corresponds to the phase  
274 closer to spring tide conditions, characterized by stronger isopycnal displacements, while LT corresponds to the phase farther  
275 from spring tide conditions, with reduced vertical displacements. These definitions are relative within each observation  
276 window and account for local stratification conditions.

$$\Delta P_{\rho_0, \rho_1, Tides} = \langle P \rangle_{\rho_0, \rho_1, HT} - \langle P \rangle_{\rho_0, \rho_1, LT} \quad (4)$$

277 The comparison between periods of strong (HT) and weak (LT) tidal forcing, relating to spring tides / neap tides cycle,  
278 conducted in a region with similar hydrodynamic properties but primarily differentiated by the intensity of ITs (HT), served  
279 as a proxy for quantifying the influence of ITs on turbulent chlorophyll-a fluxes.

a mis en forme: Police :+Titres CS (TimesNew Roman)

a mis en forme: Police :+Titres CS (TimesNew Roman)

a mis en forme: Police :+Titres CS (TimesNew Roman)

a mis en forme: Police :+Titres CS (TimesNew Roman)  
a mis en forme: Retrait : Avant: 0 cm, Première ligne: 0 cm

a mis en forme: Police :+Titres CS (TimesNew Roman)

a mis en forme: Police :Cambria Math

a mis en forme: Police :+Titres CS (TimesNew Roman)

a mis en forme: Police :+Titres CS (TimesNew Roman)

a mis en forme: Police :+Titres CS (TimesNew Roman)

a mis en forme: Police :+Titres CS (TimesNew Roman)

a mis en forme: Police :+Titres CS (TimesNew Roman)

a mis en forme: Police :+Titres CS (TimesNew Roman)

a mis en forme: Police :+Titres CS (TimesNew Roman)

a mis en forme: Police :+Titres CS (TimesNew Roman)

281 We divided the water column into three isopycnal layers: the surface layer, the Deep Chlorophyll Maximum (DCM) layer,  
 282 and the bottom layer. We assumed that the difference of mean  $\text{CHL}_{\text{chlorophyll-a}}$  integrated in DCM at an isopycnal layer  
 283 around the DCM, defined here as  $\Delta\text{CHL}_{\text{DCM}}$ , the change in depth-integrated chlorophyll-a, in  $\text{mg m}^{-2}$ , within the DCM  
 284 ( $\Delta\text{Diff}_{\text{DCM}}$ , layer attributable to turbulent diffusive fluxes) is redistributed upward and downward through mixing such that their  
 285 sum equals  $\Delta\text{Diff}_{\text{DCM}} = \Delta\text{CHL}_{\text{DCM}}$ , with proportions  $n$  for the surface layer and  $m$  for the bottom layer, where  $n+m=1$ .  
 286 This assumption is consistent with recent observations in our study area showing that internal tides dominate vertical mixing  
 287 over the Amazon shelf break (Kouogang et al., 2025). Using this partitioning approach, we express the variation in chlorophyll-a ( $\Delta\text{CHL}$ ) for each layer as follows:

$$\Delta\text{CHL}_{\text{SURF}} = -n \cdot \Delta\text{Diff}_{\text{DCM}} + \Delta\text{SMS}_{\text{SURF}} \quad (5)$$

$$\Delta\text{CHL}_{\text{DCM}} = \Delta\text{Diff}_{\text{DCM}} + \Delta\text{SMS}_{\text{DCM}} \quad (6)$$

$$\Delta\text{CHL}_{\text{DEEP}} = -m \cdot \Delta\text{Diff}_{\text{DCM}} + \Delta\text{SMS}_{\text{DEEP}} \quad (7)$$

292 With  $-n \cdot \Delta\text{Diff}_{\text{DCM}} = \Delta\text{Diff}_{\text{SURF}}$  and  $-m \cdot \Delta\text{Diff}_{\text{DCM}} = \Delta\text{Diff}_{\text{DEEP}}$ ,

293 By summing Equations 5, 6, and 7, the diffusion-related component cancels out, leaving:

$$\Delta\text{SMS}_{\text{DCM}} + \Delta\text{SMS}_{\text{Surf}} + \Delta\text{SMS}_{\text{Deep}} = \Delta\text{CHL}_{\text{TOT}} \quad (8)$$

295 The total chlorophyll-a variation  $\Delta\text{CHL}_{\text{TOT}}$  between high tide (HT) and low tide (LT) periods is interpreted as follows:  
 296 if  $\Delta\text{CHL}_{\text{TOT}} > 0$  this value represents the minimum possible net production. Respectively if  $\Delta\text{CHL}_{\text{TOT}} < 0$  it indicates a  
 297 dominance of grazing

a mis en forme: En-tête

a mis en forme: Police :+Titres CS (TimesNew Roman), Anglais (États-Unis)

a mis en forme: Police :+Titres CS (TimesNew Roman), Anglais (États-Unis)

a mis en forme: Police :+Titres CS (TimesNew Roman), Anglais (États-Unis)

a mis en forme: Police :+Titres CS (TimesNew Roman), Anglais (États-Unis)

a mis en forme: Police :+Titres CS (TimesNew Roman), Anglais (États-Unis)

a mis en forme: Police :+Titres CS (TimesNew Roman), Anglais (États-Unis)

a mis en forme: Police :+Titres CS (TimesNew Roman), Anglais (États-Unis)

a mis en forme: Police :+Titres CS (TimesNew Roman), Anglais (États-Unis)

a mis en forme: Police :+Titres CS (TimesNew Roman), Français (France)

a mis en forme: Police :+Titres CS (TimesNew Roman), Anglais (États-Unis)

a mis en forme: Police :+Titres CS (TimesNew Roman)

a mis en forme: Police :+Titres CS (TimesNew Roman), Français (France)

a mis en forme: Police :+Titres CS (TimesNew Roman), Français (France)

a mis en forme: Police :+Titres CS (TimesNew Roman), Français (France)

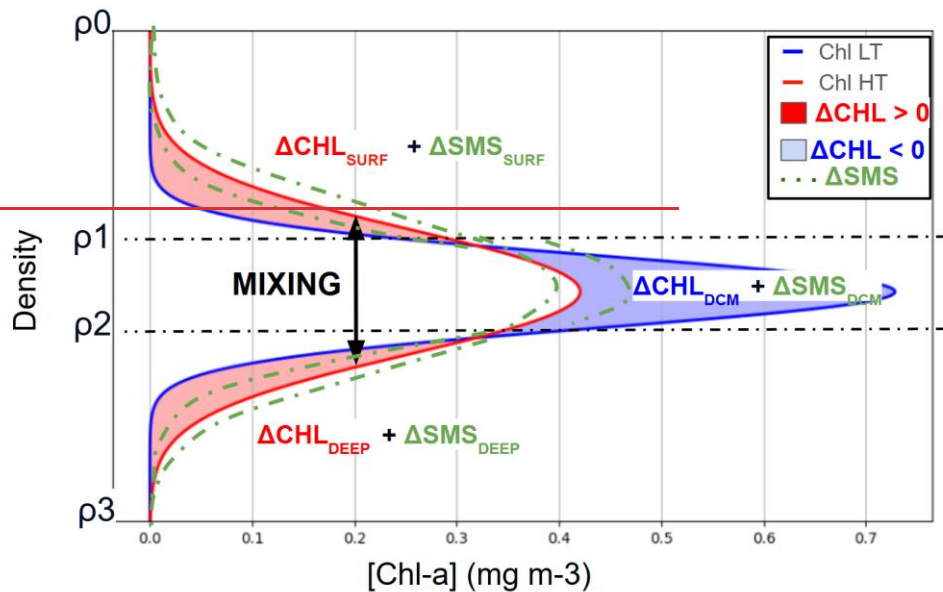
a mis en forme: Police :+Titres CS (TimesNew Roman), Français (France)

a mis en forme: Police :+Titres CS (TimesNew Roman), Français (France)

a mis en forme: Police :+Titres CS (TimesNew Roman), Français (France)

a mis en forme: Police :+Titres CS (TimesNew Roman), Français (France)

a mis en forme: Police :+Titres CS (TimesNew Roman), Français (France)



298  
299 Figure 2 : Schematic of Vertical diffusion of chlorophyll-a Peak between LT period (blue) vs HT period (red) with profile  
300 modification due to ITs mixing

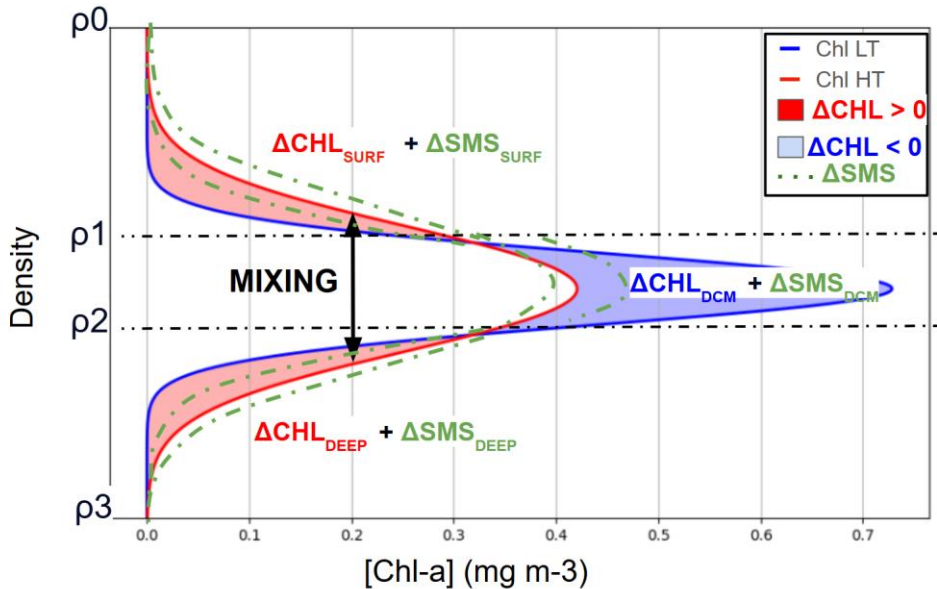


Figure 2 : Schematic representation of vertical chlorophyll-a distribution during Low Tidal Forcing (LT, blue) and High Tidal Forcing (HT, red) periods, illustrating profile modifications induced by internal tide-driven mixing. Red shading ( $\Delta\text{CHL} > 0$ ) indicates chlorophyll-a increases, blue shading ( $\Delta\text{CHL} < 0$ ) indicates decreases, and green shading denotes the potential range of variation in chlorophyll-a attributable to SMS (biological sources and sinks), which can either increase or decrease chlorophyll-a concentrations.

### 2.2.3 Statistical Analysis

In this study, various statistical methods were employed to analyse the impact of ITs on chlorophyll-a distribution across density layers. The Mann-Whitney U test, a non-parametric test, was selected to compare chlorophyll-a concentrations between periods of high and low ITs within different density layers. This test is particularly suitable here, as it does not require the assumption of data normality distribution, which is often difficult to ensure for environmental samples with irregular distributions. Mean comparisons and percentage changes provide a statistical approach of ITs on chlorophyll-a. Maximum chlorophyll-a concentrations and DCM thickness were extracted from fluorescence profiles. A Pearson-Spearman ranked correlation analysis was performed to assess the relationship between these variables. Statistical significance was determined using the associated p-value. Additionally, descriptive statistics by isopycnal layer were calculated for each density zone,

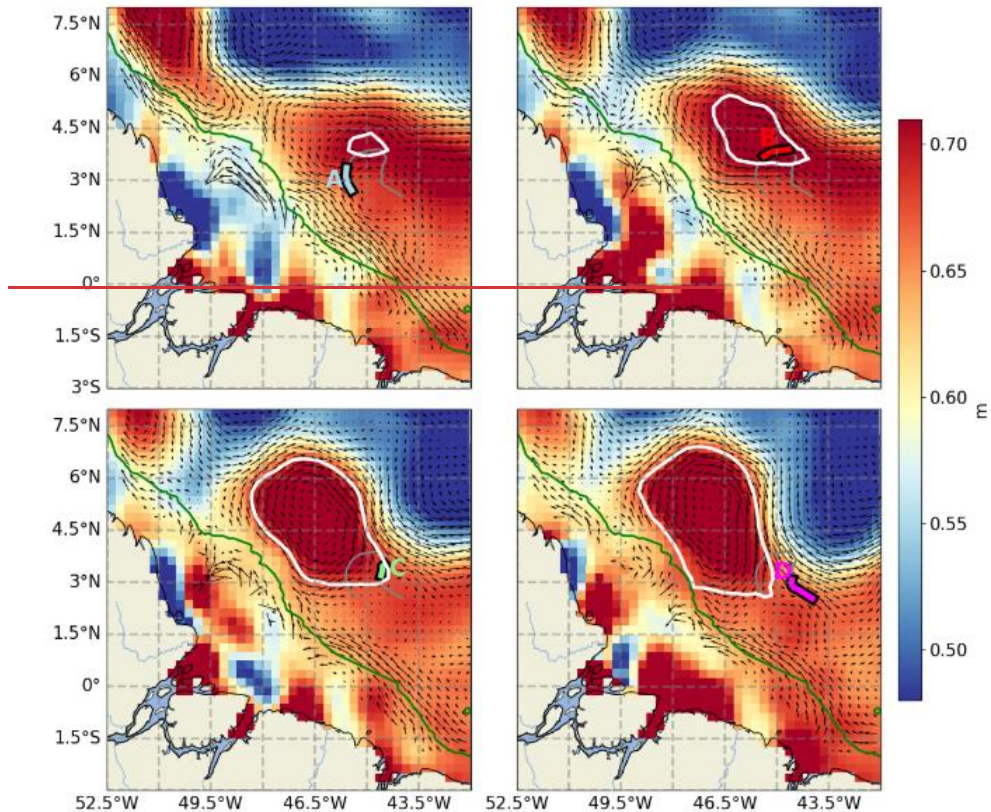
316 offering a detailed view of trends specific to layers and enabling the identification of significant changes. Collectively, these  
317 methods robustly capture significant differences and their potential effects on chlorophyll-a distribution and concentration.

318 **3 Results**

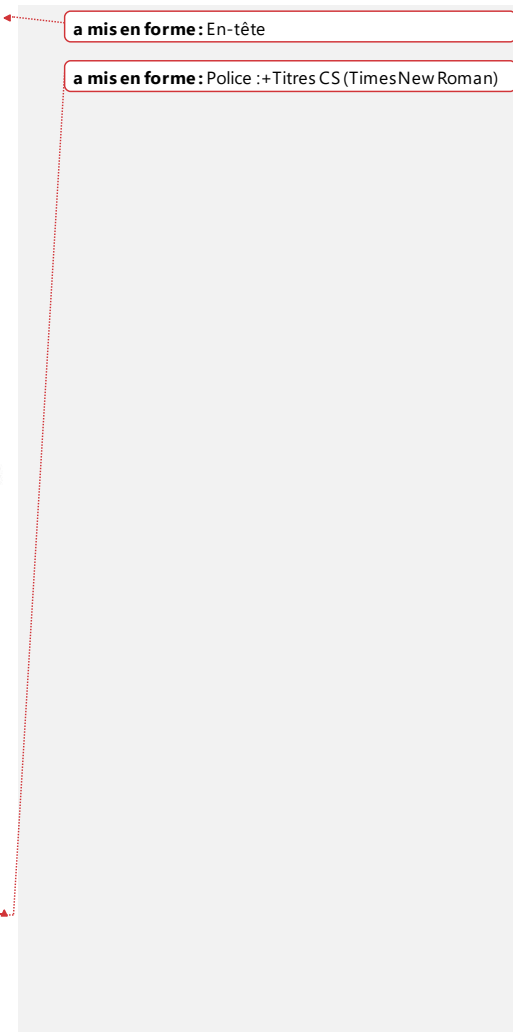
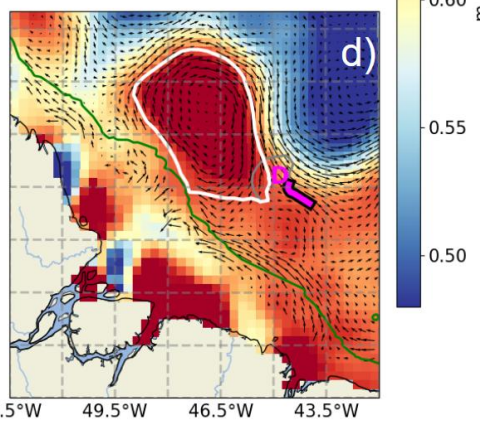
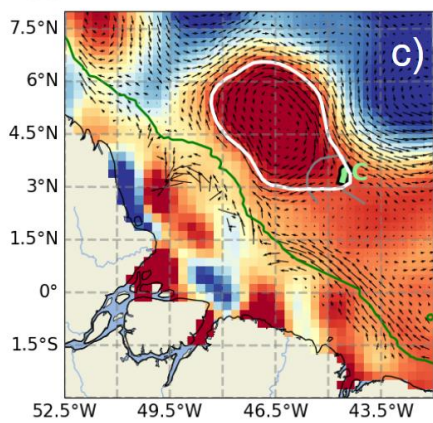
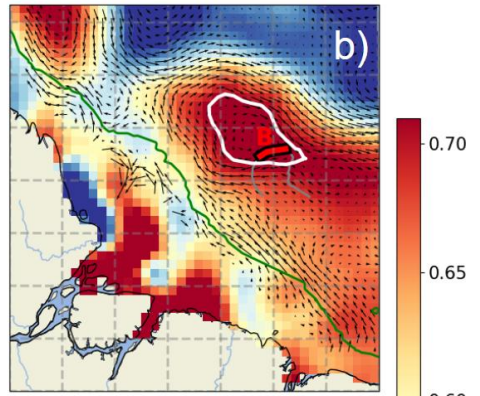
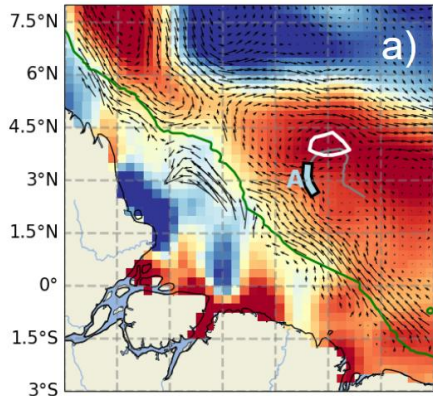
319 **3.1 The glider study area**

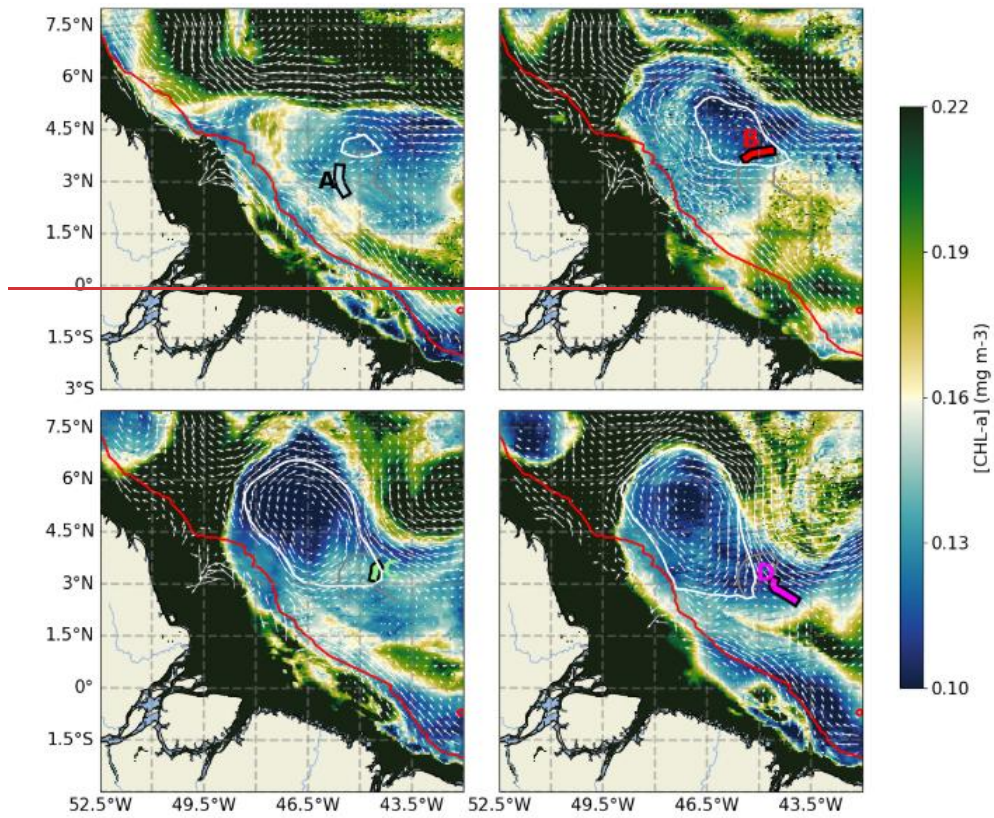
320 The oceanic circulation in the study area was dominated by two major current systems: the NBC and the NECC. Their  
321 interaction was regulated by the seasonal retroflection of the NBC, as that was clearly illustrated in the Absolute Dynamic  
322 Topography (ADT) maps (Fig. 3a–d). This circulation was associated with ADT values reaching approximately 0.6 m. From  
323 a biogeochemical perspective, strong contrasts were observed between offshore waters and the Amazon continental shelf.  
324 The offshore waters were characterized by oligotrophic conditions, with low chlorophyll-a concentrations (~0.1 mg m<sup>-3</sup>),  
325 whereas the Amazon shelf was dominated by turbid waters, rich in suspended matter, with chlorophyll-a concentrations  
326 exceeding 1 mg m<sup>-3</sup>. (Fig. 3e-h). This gradient highlighted the significant influence of the Amazon plume on local  
327 productivity. Moreover, the depth of the euphotic layer (Zeu) (Fig. 4, purple) remained relatively stable varied along the  
328 glider transect, ranging between 72 m showing a decrease in the eddy core and 87 m.

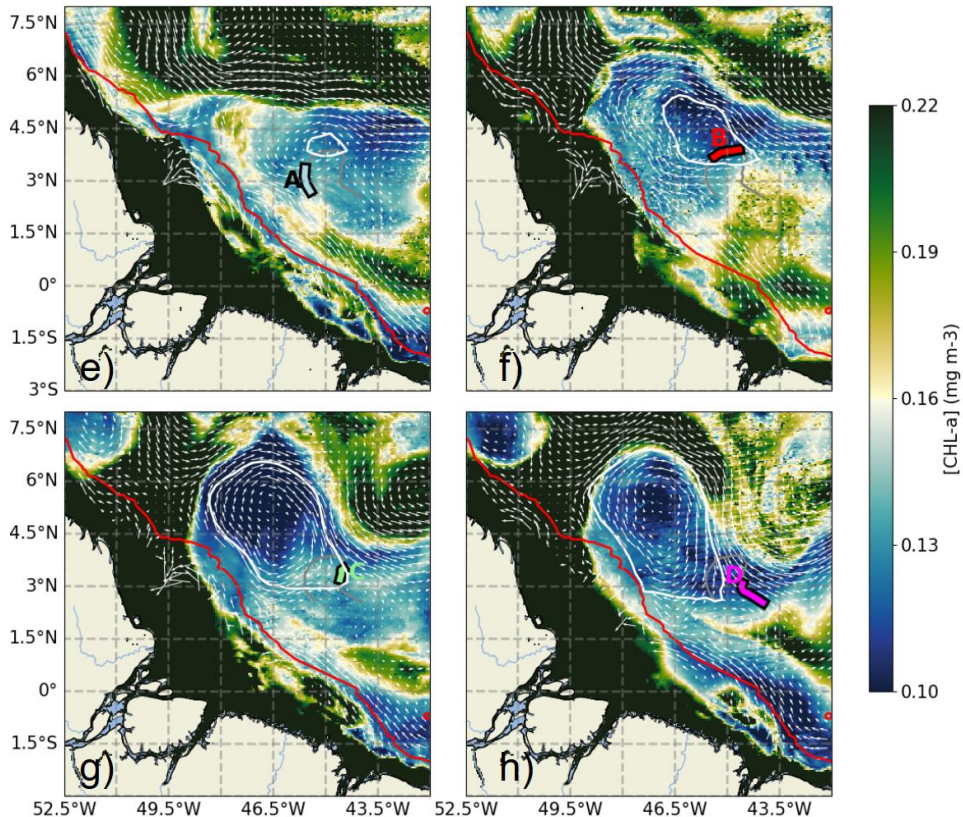
a mis en forme: Police :+Titres CS (TimesNew Roman)  
a mis en forme: Police :+Titres CS (TimesNew Roman)  
a mis en forme: Police :+Titres CS (TimesNew Roman)  
a mis en forme: Police :+Titres CS (TimesNew Roman)  
a mis en forme: Police :+Titres CS (TimesNew Roman)  
a mis en forme: Police :+Titres CS (TimesNew Roman)



an increase toward its periphery, following a pattern similar to that observed for chlorophyll-a.







333  
334 **Figure 3.** (a–d) Absolute Dynamic Topography (ADT) maps for September 11 (a), 16 (b), 22 (c), and 28 (d), 2021. (e–h) Satellite-  
335 derived surface chlorophyll-a maps for the same dates: September 11 (e), 16 (f), 22 (g), and 28 (h). The AE1 eddy is outlined by white  
336 ovals. The glider trajectory is shown as a grey line, with color-coded segments indicating periods A, B, C, and D (as defined in Fig.  
337 1). Geostrophic surface currents are shown as arrows. The 1000 m isobath is marked in green (a–d) and red (e–h).

a mis en forme: Police :+Titres CS (TimesNewRoman)

338 *Formation and Evolution of the Anticyclonic Eddy (AE1)*

339 On Sept 11st 2021, an anticyclonic eddy (AE1) formed in the region, identified by an ADT peak reaching approximately 0.7  
340 m (Fig. 3a, white circle). The eddy core gradually migrated from 44.5°W-4°N to 47.5°W-5.5°N over the following 27 days,

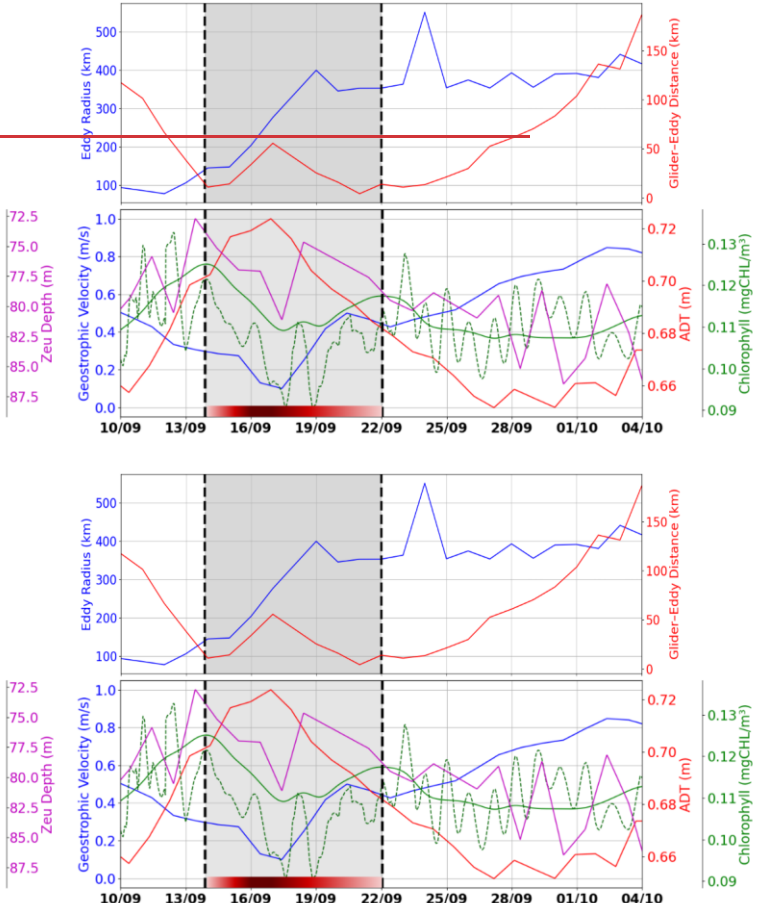
341 covering roughly 372 km with an average speed of 0.16 m/s. Between Sept 12nd and Sept 19th, the eddy underwent significant  
 342 expansion, with its radius increasing from 100 km to approximately 400 km.

343 *Glider-Eddy Interactions*

344 The influence of the eddy on surface velocity is evident from an initial decrease in speed from 0.58 m/s to 0.17 m/s in Sept  
 345 17th, followed by a gradual acceleration reaching 0.8 m/s at the end of the transect (Fig. 4, bottom panel). Between Sept 14th  
 346 and Sept 22nd, as the glider traversed the eddy, variations in its distance from the eddy's outer boundary were observed (Fig.  
 347 4, top panel). These fluctuations confirm that the glider remained along the eddy's periphery, highlighting the kinematic effects  
 348 induced by its circulation. Maximum geostrophic velocities, derived from ADT gradients, further indicate intense eddy  
 349 dynamics, with circulating currents reaching up to 0.8 m/s toward the end of the observation period.

350 *Biogeochemical Characteristics Associated with AE1*

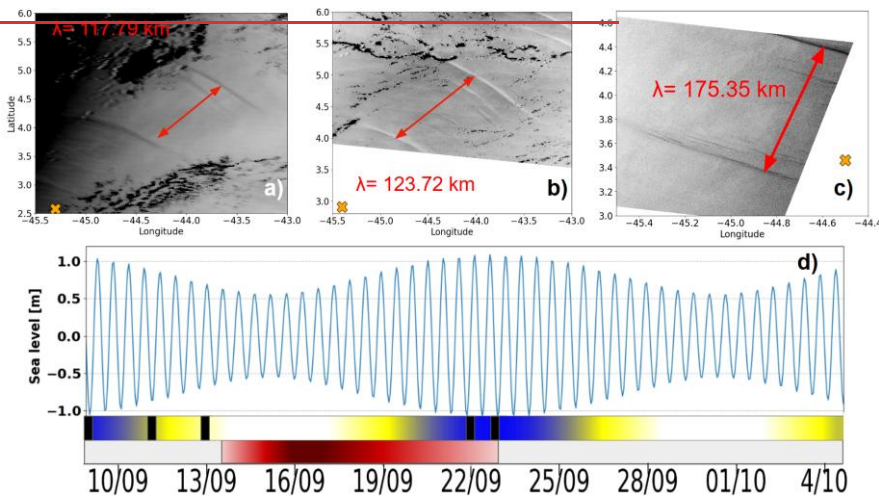
351 The lowest Chlorophyll values (~0.11 mg m<sup>-3</sup>) along the glider acquisition were recorded in the eddy core, which was  
 352 characterized by minimal velocities and maximum Absolute Dynamic Topography (ADT). In contrast, higher biological  
 353 activity was observed at the eddy's periphery, marked by dashed black lines on September 14 and Sept 22<sup>nd</sup> (Fig. 4),  
 354 emphasizing the spatial heterogeneity induced by the eddy's circulation. This pattern was explained by the typical behaviour  
 355 of anticyclonic eddies, where isopycnal depression inhibited the upward flux of nutrients, thereby limiting primary  
 356 productivity. The coupling between the eddy's physical dynamics and the distribution of biological parameters was highlighted  
 357 by the chlorophyll-a maps. During the eddy-impacted period (shaded in grey), both glider (dashed green) and satellite (solid  
 358 green) chlorophyll-a data show a decrease at the eddy center (Sept 16th – Sept 19th) and an increase at its edge (Sept 14<sup>th</sup> and  
 359 Sept 22<sup>nd</sup>). In addition to the smoother satellite signal, the glider data reveal short-term oscillations; these high-frequency  
 360 variations, likely associated with diurnal and semidiurnal processes, are not resolved by satellite observations, although the  
 361 satellite successfully captures the overall trend and order of magnitude.

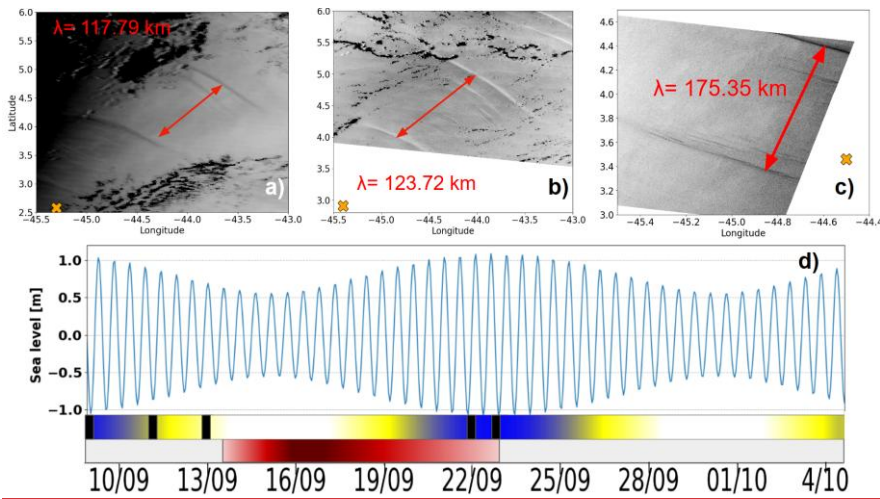


363  
364 **Figure 4:** (Top) Time series of the distance between the glider and the nearest eddy contour (red) and the maximum eddy radius (blue). (Bottom) Geostrophic velocity magnitude along the glider's track (blue), ADT along the glider's track (red), chlorophyll-a concentration along the glider's track from GlobColour (solid green), integrated chlorophyll-a between surface and Zpd from glider (dashed green), euphotic depth along the glider's track (purple). The red segment represents AE1, with shading that becomes  
365 lighter towards the edge and darker at the core  
366  
367  
368  
369

## 370 Internal Solitary Waves

371 During the observation period, between Sept 9<sup>th</sup> and Sept 23<sup>rd</sup> 2021, a total of 12 internal solitary wave (ISW) ~~crests waves~~  
 372 ~~packet~~ were identified (Table 1). These waves were detected through a combination of satellite observation and in situ glider  
 373 measurements, enabling documentation of their occurrence and dynamics over a two-week period. Satellite images (Fig. 5a-  
 374 c), acquired on Sept 9<sup>th</sup> and Sept 11<sup>th</sup> (sunglint information) and on Sept 23<sup>rd</sup> (SAR imagery), revealed the surface signatures  
 375 of internal solitary waves. The glider's position, marked by an orange cross on the images, confirms the influence of intense  
 376 ISWs during its evolution. Figure 5d illustrates the tidal current amplitudes derived from the FES2014 model (Lyard et al.,  
 377 2014) at the point (46°W-0.5°N). The graph highlights the variations between spring tides (blue-shaded areas) and neap tides  
 378 (white areas), as well as transitional phases (yellow). The black rectangles in Fig. 5d, indicating the occurrences of solitons,  
 379 show a clear alignment between the presence of internal wave trains and spring tide periods, as also shown by De Macedo et  
 380 al. (2023). The observed waves primarily propagated towards the northeast, with wavelengths ranging from 117 km to 175  
 381 km, characteristic of mode-1 internal waves. These structures exhibit rapid dynamics, with estimated propagation speeds of  
 382 approximately 3 m/s (De Macedo et al., 2023), significantly faster than the average speed of the glider (~0.14 m/s). This speed  
 383 difference justifies that the glider is unable to capture the same wave crest more than once, and is almost stationary in the ITs  
 384 field (reduced aliasing).





386  
387 **Figure 5:** (a-c) Satellite imagery acquired on September 9, 2021, at 13:45 UTC, and September 11, 2021, at 13:30 UTC (both from  
388 sunglint imagery), as well as on September 23, 2021, at 08:47:35 UTC (SAR imagery). (d) Tidal current amplitudes derived from  
389 the FES2014 model (Lyard et al., 2021) at point (46°W, 0.5°N). The orange cross denotes the glider's position at the corresponding  
390 timestamp. The timeline illustrates the variation of Spring Tides (blue), Neap Tides (White), transient zone (Yellow). The red  
391 segment represents AE1, with shading that becomes lighter towards the edge and darker at the core.

a mis en forme: Police :+Titres CS (TimesNewRoman)

392 **Table 1:** Internal solitary waves detected by SAR (Sentinel-1) and/or Sunglint (Modis) during the period Sept 9<sup>th</sup> to Oct 5<sup>th</sup> off Amazon  
393 shelf-break region

Date	Sensor Type	CrestWave Packet detected
Sept 9 <sup>th</sup> 2021	MODIS	1
Sept 11 <sup>st</sup> 2021	Sentinel-1	3
	MODIS	1
Sept 13 <sup>rd</sup> 2021	MODIS	4
Sept 22 <sup>nd</sup> 2021	MODIS	1
Sept 23 <sup>rd</sup> 2021	Sentinel-1	2

a mis en forme: En-tête

a mis en forme: Police :+Titres CS (TimesNew Roman)

a mis en forme le tableau

a mis en forme: Police :+Titres CS (TimesNew Roman)

a mis en forme: Police :+Titres CS (TimesNew Roman)

a mis en forme: Police :+Titres CS (TimesNew Roman)

a mis en forme: Police :+Titres CS (TimesNew Roman)

a mis en forme: Police :+Titres CS (TimesNew Roman)

a mis en forme: Police :+Titres CS (TimesNew Roman)

394

### 3.2 Physical Near Surface Processes

#### Transect Divided into Four Periods

To assess the impact of ITs on chlorophyll-a, the transect was divided into distinct periods based on hydrographic criteria, ensuring a robust comparative framework. The relevance of this classification (A, B, C, and D) was validated using T/S diagrams (Fig. 7), where four distinct hydrographic profiles were identified. Period A (Sept 9<sup>th</sup> – Sept 13<sup>rd</sup>, Blue) was characterized by a strong salinity gradient above 23.5 kg/m<sup>3</sup>, ranging from 36.2 to 36.6, while temperature remained stable around 28°C. This period was observed at edge of the NBC (Fig. 1, Fig. 3), with a total distance of 96.69 km covered by the glider. Period B (Sept 15–19, Red) was located within (AE1). During this phase, the glider covered a distance of 84.20 km. Period C (Sept 22<sup>nd</sup>–25<sup>th</sup>, Green) was identified as a transition zone between B and D, exhibiting a structure similar to Period B in the 23.3–24 kg/m<sup>3</sup> layer but with a saltier water mass in the 24–24.8 kg/m<sup>3</sup> range. Period D (Sept 28<sup>th</sup>–Oct 5<sup>th</sup>, Black) was associated with waters in the influence of the North Equatorial Countercurrent (NECC) (Fig. 1, Fig. 3), where the T/S profile revealed three distinct layers within the 0–200 m column. The surface layer (23–23.3 kg/m<sup>3</sup>) was stratified in temperature while salinity remained constant (~36.3). Beneath it, an intermediate transition layer (23.3–23.7 kg/m<sup>3</sup>) was marked by coherent T and S gradients, followed by a deep layer, where temperature remained stratified, and salinity was stable (~36.5). This classification was found to effectively capture the hydrographic variability along the transect, providing a general frame for analysing internal tide dynamics.

a mis en forme: Police :+Titres CS (TimesNew Roman), Non Italique

a mis en forme: Normal, EspaceAvant: 0 pt, Après: 0 pt, Interligne : simple

a mis en forme: Police :+Titres CS (TimesNew Roman)

a mis en forme: Police :+Titres CS (TimesNew Roman)

a mis en forme: Police :+Titres CS (TimesNew Roman)

a mis en forme: En-tête

412

### 413 *Near Surface Hydrography*

414 The hydrographic observations collected by the glider between the surface and 200 m depth reveal a strongly stratified  
415 thermohaline structure, characteristic of tropical waters (Fig. 6). The temperature (T), salinity (S), and density ( $\sigma_0$ ) profiles  
416 indicated the presence of a homogeneous layer between 0 and 50 m, followed by a thermocline, halocline, and pycnocline  
417 extending from 50 to 160 m. Salinity above 35.5 in this region indicates euhaline conditions, showing the plume did not affect  
418 the southern area. Notable hydrographic changes are further observed during the study period. Between Sept 14<sup>th</sup> and Sept  
419 22<sup>nd</sup>, as the glider crossed AE1 (marked by ~~circular areas in black lines~~, Fig. 3a), a lenticular and homogeneous isopycnal field  
420 was detected, with nearly uniform temperature (27°C) and salinity (36.5) between isopycnals 23.5 and 23.7 (75m–125m depth).  
421 At the surface, this anticyclone exhibited warmer and more stratified waters compared to the surrounding environment, while  
422 salinity remained homogeneous. Prior to crossing AE1, the glider was deployed at the edge of the NBC (Fig. 1, Fig. 3a) from  
423 September 9<sup>th</sup> to 14<sup>th</sup>. In contrast, this region displayed a homogeneous temperature layer but a stratified salinity profile. During  
424 this period, a maximum salinity zone (~36.7) was observed between 120 and 150 m depth, generally associated with the  
425 maximum salinity transport by the North Brazil Current (NBC) (Silva et al., 2009), which was significantly reduced in  
426 subsequent periods indicating the shift in background conditions. Between September 22<sup>nd</sup> and 28<sup>th</sup>, the region was  
427 characterized by a homogeneous surface layer (0–50 m) in both temperature and salinity, accompanied by a pronounced uplift  
428 of the 23.10 isopycnal. Below 50 m, the ocean became increasingly stratified, exhibiting coherent variations in T and S. From  
429 Sept 28<sup>th</sup> to Oct 4<sup>th</sup>, the glider entered the waters of the North Equatorial Countercurrent (NECC), characterized by an  
430 accelerated geostrophic current field (Fig. 4, bottom), reaching speeds of 0.6 m/s eastward. The hydrography during this period  
431 revealed the warmest surface layer of the transect (~30°C), followed by a coherent stratification in T and S. The four distinct  
432 regions, identified through these hydrographic variations, have been designated as A, B, C, and D, while the edges have been  
433 excluded, as they are considered transition periods.

434

435

436

437

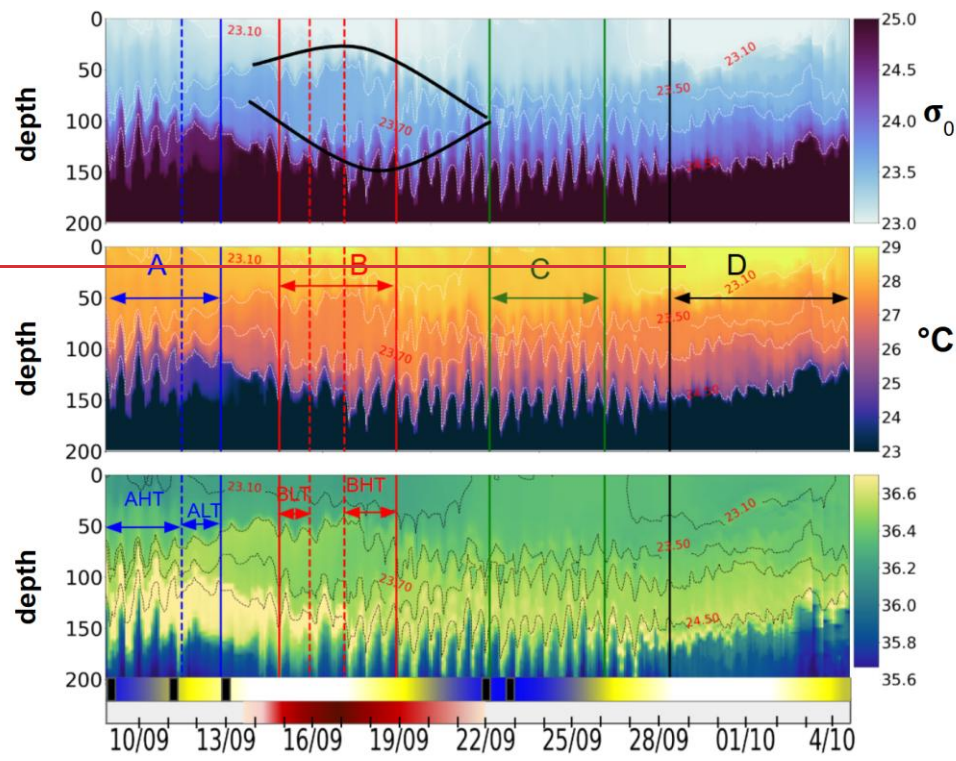
a mis en forme: Police :+Titres CS (TimesNew Roman)

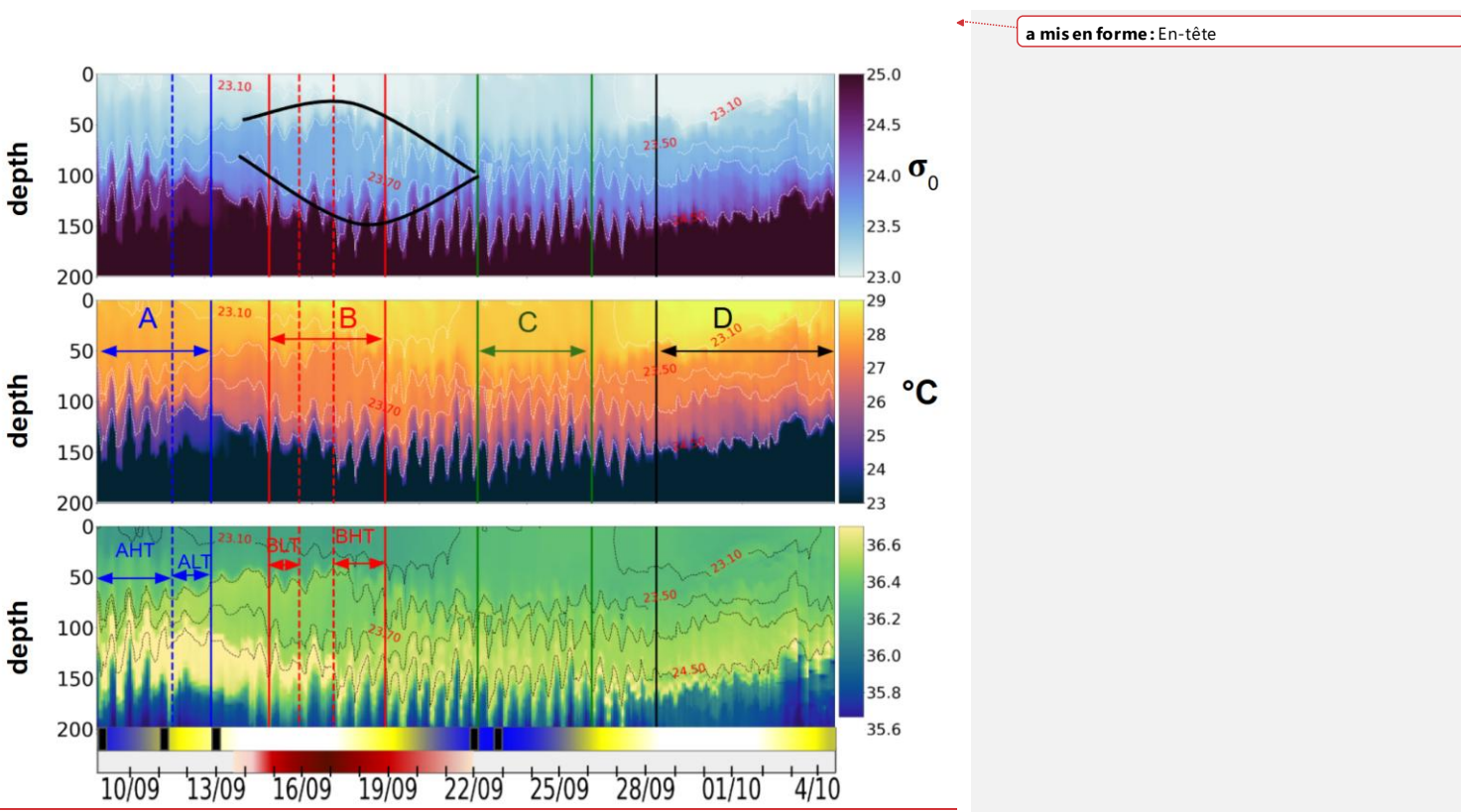
a mis en forme: Police :CambriaMath

a mis en forme: Police :+Titres CS (TimesNew Roman)

a mis en forme: Police :+Titres CS (TimesNew Roman)

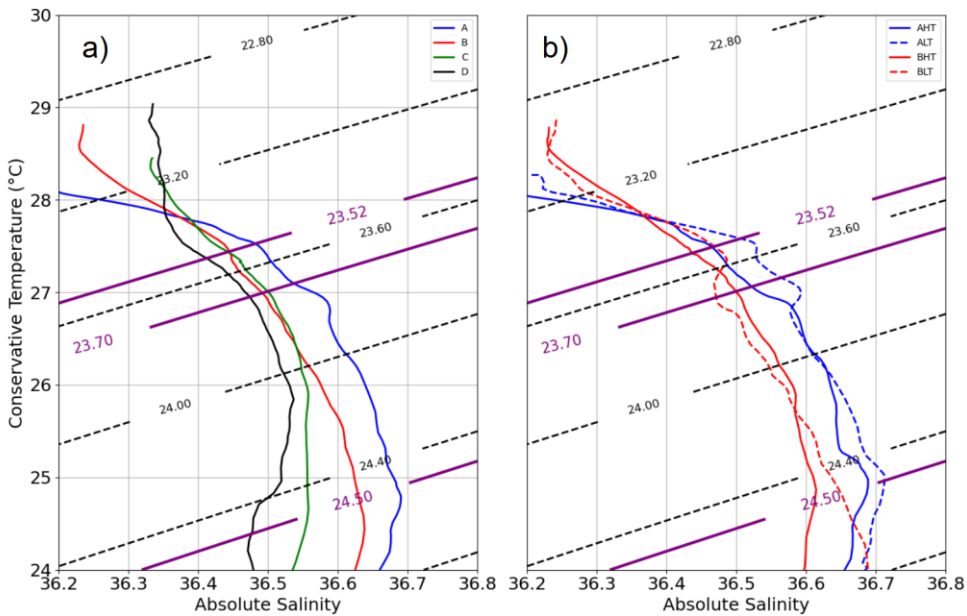
a mis en forme: En-tête





439  
440 **Figure 6:** Hovmöller diagrams showing (a)  $\sigma_0$  density (with the black lens highlighting eddy AE1 as identified in Section 3.1), (b)  
441 Conservative Temperature, and (c) Absolute Salinity, all derived from glider observations. The timeline below the plots indicates  
442 key oceanographic processes discussed in Section 3.1: blue segments mark spring tide events, white indicates neap tides, and the red  
443 segment corresponds to AE1, with shading intensity increasing from lighter at the periphery to darker at the core. A black rectangle  
444 marks the occurrence of internal solitary waves (ISWs) detected from satellite data. Labels A, B, C, and D denote distinct periods,  
445 A and B further divided into high tide (HT) and low tide (LT) subperiods, reflecting variations in tidal intensity.

a mis en forme: Police :+Titres CS (TimesNewRoman)



446 **Transsect Divided into Four Periods**

447 To assess the impact of ITs on chlorophyll *a*, the transect was divided into distinct periods based on hydrographic criteria,  
 448 ensuring a robust comparative framework. The relevance of this classification (A, B, C, and D) was validated using T/S  
 449 diagrams (Fig. 7), where four distinct hydrographic profiles were identified. Period A (Sept 9<sup>th</sup>–Sept 13<sup>rd</sup>, Blue) was  
 450 characterized by a strong salinity gradient above 22.52 kg/m<sup>3</sup>, ranging from 36.2 to 36.6, while temperature remained stable  
 451 around 28°C. This period was observed at edge of the NPC (Fig. 1, Fig. 2), with a total distance of 6.60 km covered by the  
 452 plume. Period B (Sept 15–19, Red) was located within (AE1), where a well-defined T/S stratification was observed, indicating  
 453 a stable water mass structure. During this phase, a distance of 84.20 km was recorded. Period C (Sept 22<sup>nd</sup>–25<sup>th</sup>, Green) was  
 454 identified as a transition zone between B and D, exhibiting a structure similar to Period B in the 22.3–24 kg/m<sup>3</sup> layer but with  
 455 a salter water mass in the 24–24.8 kg/m<sup>3</sup> range. Period D (Sept 28<sup>th</sup>–Oct 5<sup>th</sup>, Black) was associated with waters in the influence  
 456 of the North Equatorial Countercurrent (NECC) (Fig. 1, Fig. 2), where the T/S profile revealed three distinct layers within the  
 457 0–200 m column. The surface layer (23–23.2 kg/m<sup>3</sup>) was stratified in temperature while salinity remained constant (~36.2).  
 458 Beneath it, an intermediate transition layer (23.3–23.7 kg/m<sup>3</sup>) was marked by coherent T and S gradients, followed by a deep

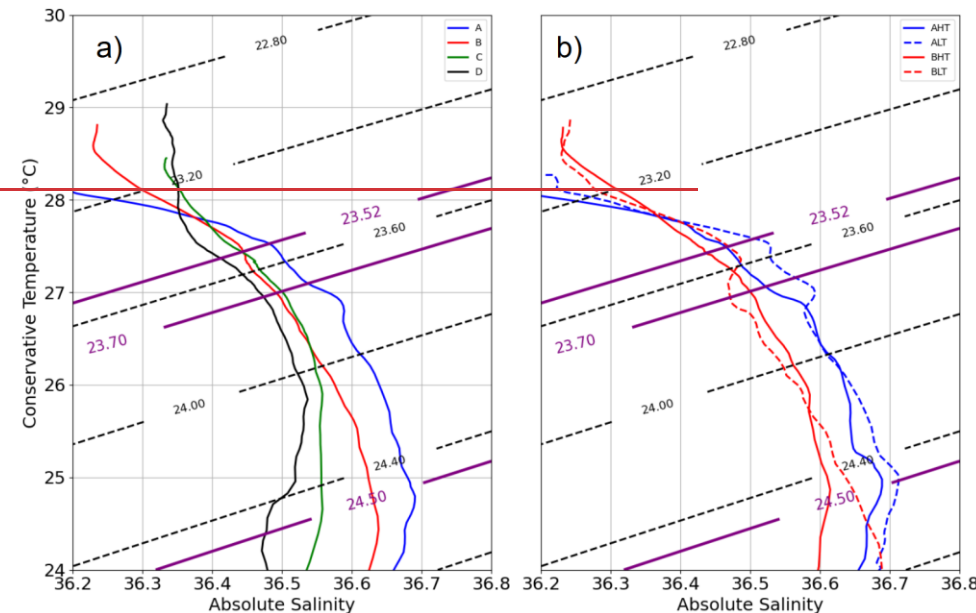
459 a mis en forme : Police :+Titres CS (TimesNew Roman)  
 a mis en forme : Police :+Titres CS (TimesNew Roman), Non Italique

a mis en forme : Normal, EspaceAvant : 0 pt, Après : 0 pt, Interligne : simple

a mis en forme : Police :+Titres CS (TimesNew Roman)  
 a mis en forme : Police :+Titres CS (TimesNew Roman)

a mis en forme : Police :+Titres CS (TimesNew Roman)

460 layer, where temperature remained stratified, and salinity was stable (~36.5). This classification was found to effectively  
 461 capture the hydrographic variability along the transect, providing a general frame for analysing internal tide dynamics.

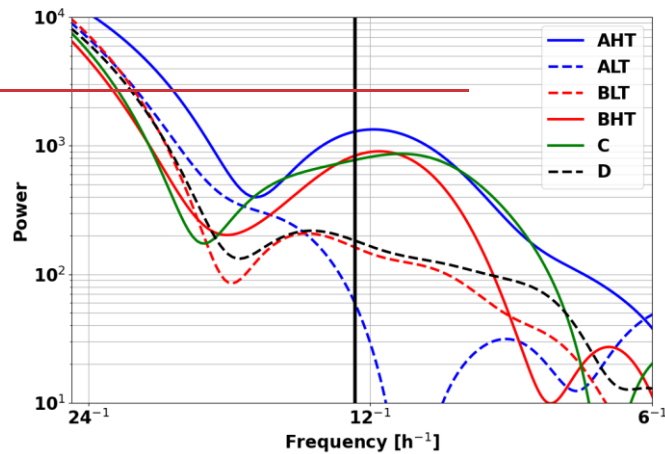


462  
 463 **Figure 7:** T/S Diagram (a - left) for periods A, B, C, and D and (b - right) for the sub-periods High Tides (HT) / Low Tides (LT)  
 464 within periods A and B. Black dotted isopycnals are plotted at intervals of 0.4 kg/m3.

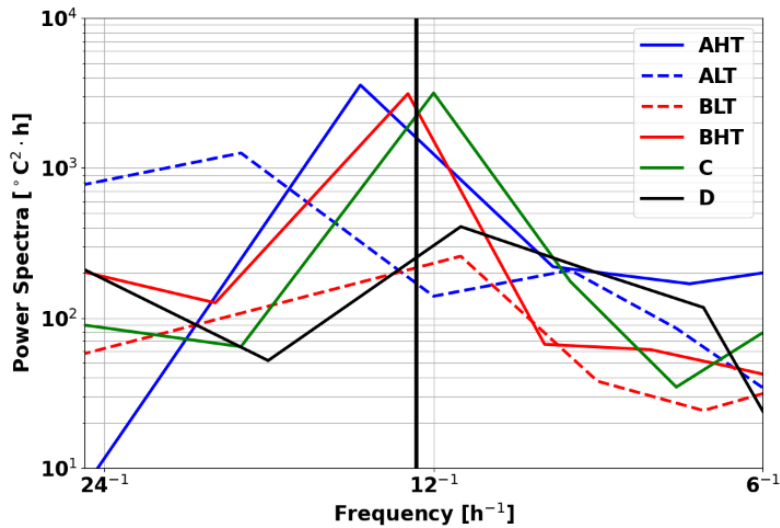
#### 465 466 *Thermocline Oscillations Driven by ITs: Variability Between High and Low Tides*

467 Thermocline oscillations were observed in all periods except D, with amplitudes ranging from 10 to 50 m and peaking near  
 468 the 24.5 isopycnal (Fig. 6). These in-phase oscillations were most intense at the pycnocline and gradually diminished toward  
 469 the surface, and were modulated by neap and spring tide cycles, with peaks coinciding with Internal Solitary Wave (ISW)  
 470 events (Fig. 5). Spring tides (A and C) induced a ~1°C temperature drop, contrasting with the surface warming in period D,  
 471 when no oscillations were detected. A Fast Fourier Transform (FFT) analysis of isotherms (145–165 m) (McInerney et al.,  
 472 2019) confirms the semi-diurnal modulation of these oscillations. Periods A and B were further divided into high Tide-  
 473 amplitude (AHT, BHT) and low Tides-amplitude (ALT, BLT) phases, while Period C exhibits continuous oscillations. All

474 showed a 12h25 spectral peak (Fig. 8) with a tenfold increase in spectral power, confirming the influence of ITs. Furthermore,  
475 Figure 7b reveals that these oscillatory phases correspond to the same water masses, validating the subdivision AHT/ALT and  
476 BHT/BLT.



477



478

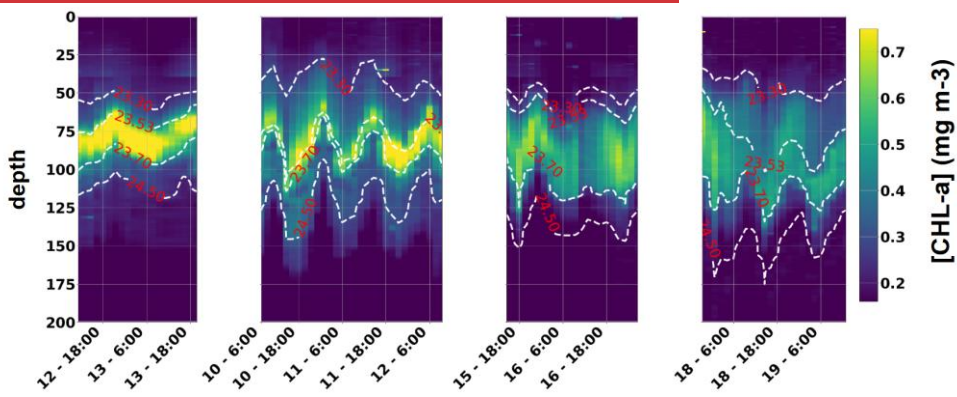
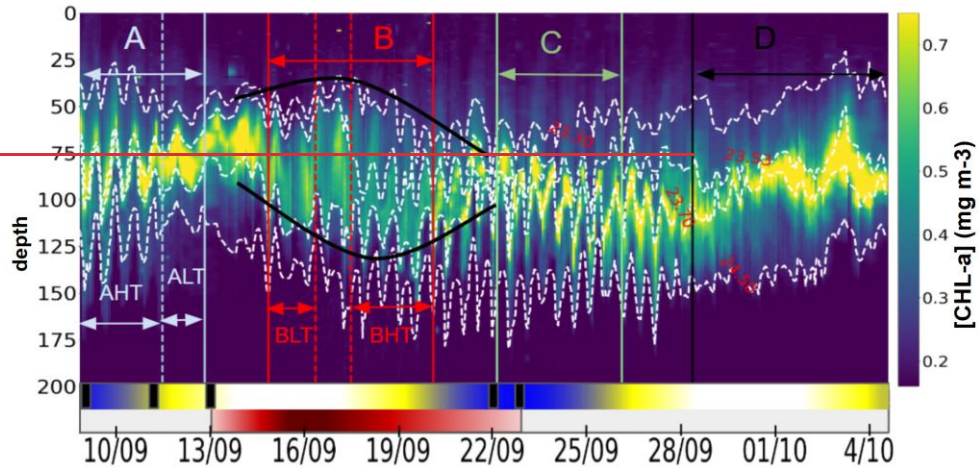
479 **Figure 8:** Spectral Analysis of temperature time series in Regions A, B, C, and D, across 145m and 165m depth.

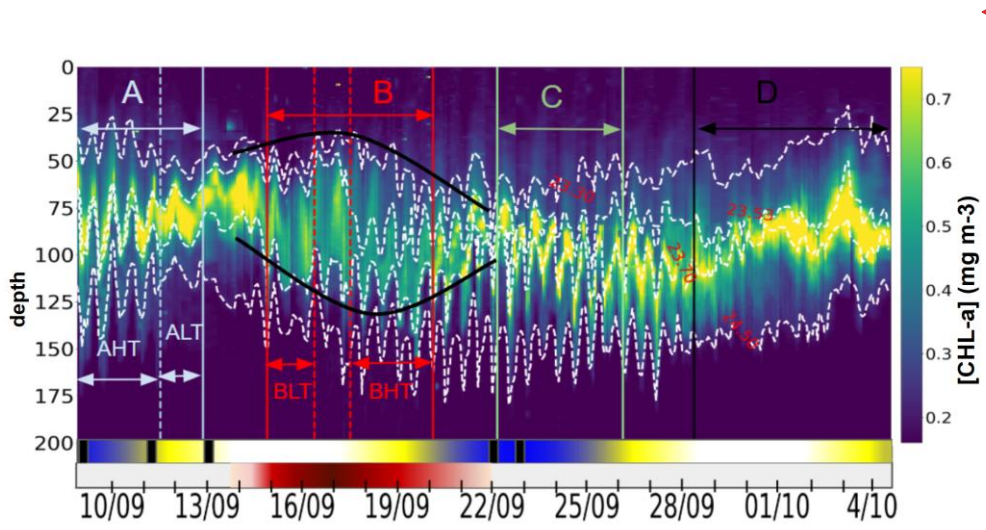
a mis en forme: Police :+Titres CS (TimesNew Roman)

### 480 3.3 ITs effect on chlorophyll

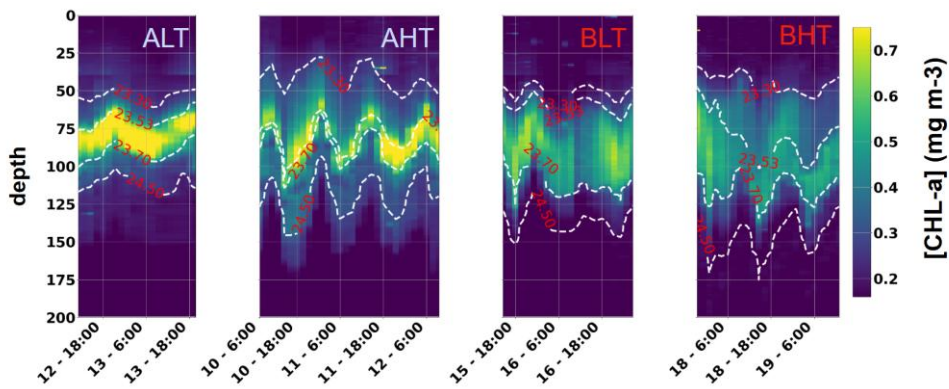
#### 481 Overview of Subsurface Processes Effects on Chlorophyll

482 The vertical distribution of chlorophyll-a along the transect (Fig. 9a) was characterized by a three-layer structure. A Deep  
 483 Chlorophyll Maximum (DCM) was observed between isopycnals 23.53 and 23.7 (corresponding to depths of approximately  
 484 70m and 120 m), with concentrations ranging from 0.4 to 0.8 mg m⁻³. The lowest value (0.4 mg m⁻³) was recorded during  
 485 period B, coinciding with the passage of the glider through the anticyclonic eddy AE1, in agreement with the surface signal  
 486 (Fig. 4, green). At the edges of AE1, a slight uplift of the DCM was observed, attributed to the upward displacement of  
 487 isopycnals. Above 23.53, a surface layer was identified, while a deeper layer extends between 23.7 and 24.5. A key finding is  
 488 the influence of ITs on the vertical structure of chlorophyll-a. The tides induced DCM oscillations with amplitudes between  
 489 15 and 45 meters at depths of 65 to 125 meters during AHT, BHT, and C, while weaker disturbances were observed during  
 490 ALT and BLT (Fig. 9b). These disturbances could impact primary production, as the light gradient is non-linear — an uplift  
 491 exposes the chlorophyll-a layer to more light than the amount lost by a downlift. The following section now focuses on the  
 492 characterization and quantification of ITs processes advection and mixing, that influence chlorophyll-a distribution.





a mis en forme: En-tête



a mis en forme: Police :+Titres CS (TimesNewRoman)

497 Figure 9: (a) Hovmöller diagram of chlorophyll-a distribution from 0 to 200 m between September 9, 2021, and October 4, 2021.  
498 Dark green segments indicate spring tide events, while light green segments correspond to neap tides. The red segment represents  
499 Anticyclonic Eddy 1 (AE1), with lighter shades at the edges and a darker core. The black rectangle highlights the presence of Internal  
500 Solitary Waves (ISWs). (b) Hovmöller diagram of chlorophyll-a from 0 to 200 m, segmented by tidal phases: ALT, AHT, BLT, and  
501 BHT.

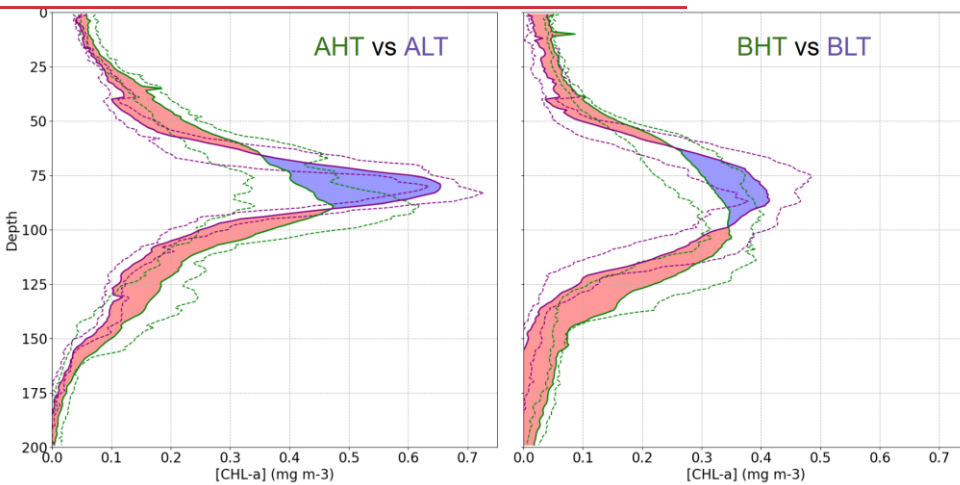
502 Variability of Chlorophyll-a Structure Between High and Low ITs

a mis en forme: En-tête

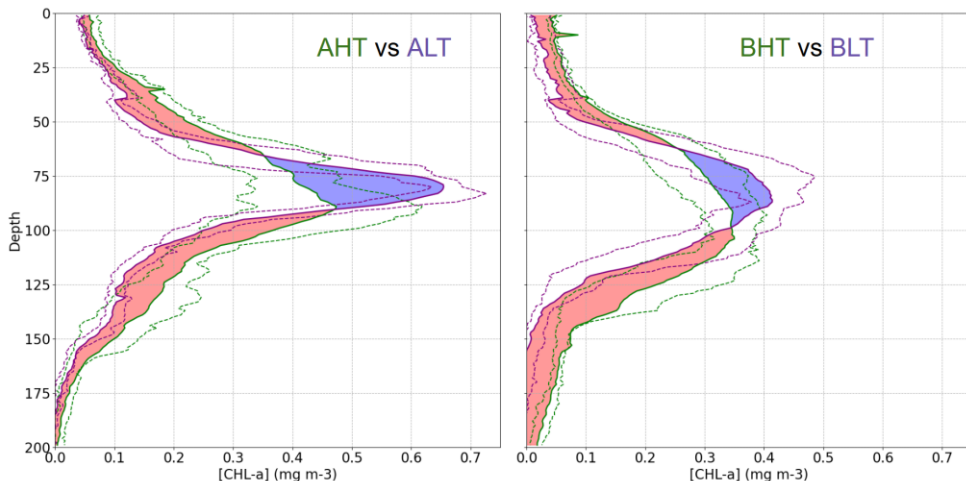
a mis en forme: Police :+Titres CS (TimesNew Roman)

504 Higher chlorophyll-a concentrations were found at the surface and in deeper layers during HT, while chlorophyll-a  
505 concentration ~~was~~ more pronounced within the DCM during LT (Fig. 10). To assess these variations and evaluate the impact  
506 of ITs on the vertical redistribution of chlorophyll, four key parameters were examined: maximum chlorophyll-a concentration,  
507 chlorophyll-a peak thickness, Total averaged chlorophyll-a content, and DCM depth (Table 2). The chlorophyll-a peak  
508 thickness corresponds to the depth range where concentrations exceed 0.2 mg m<sup>-3</sup>.

509 Under HT conditions, ~~ITs induce total averaged chlorophyll-a content increased significantly, indicating an overall~~  
510 ~~enhancement of primary production, with rises of 14% ( $\Delta\text{CHL}_{\text{total}} = 4.44 \text{ mg m}^{-2}$  where  $\Delta\text{CHL}_{\text{total}}$  is the total variation of~~  
511 ~~averaged integrated chlorophyll-a between HT and LT) in period A (resp. 29%,  $\Delta\text{CHL}_{\text{total}} = 6.98 \text{ mg m}^{-2}$  in period B. This~~  
512 ~~increase was associated with internal tide-induced~~ vertical displacements of chlorophyll, ~~leading to a redistribution of which~~  
513 ~~distributed~~ biomass across different layers. Specifically, maximum chlorophyll-a concentration decreased by 17% (0.12 mg  
514 m<sup>-3</sup>) in period A (resp. 9%, 0.04 mg m<sup>-3</sup> in period B), while the peak thickness expanded by 50% (resp. 30%). The resulting  
515 redistribution led to an inverse relationship between maximum chlorophyll-a concentration and DCM thickness (Fig. 11). This  
516 correlation was statistically significant, with Pearson coefficients of  $r = -0.4344$  ( $p = 0.01501$ ) for period A and  $r = -0.3429$  ( $p$   
517 = 0.02604) for period B. Total averaged chlorophyll-a content increased significantly during HT, with rises of 14% ( $\Delta\text{CHL}_{\text{total}}$   
518 = 4.44 mg m<sup>-2</sup> where  $\Delta\text{CHL}_{\text{total}}$  is the total variation of averaged integrated chlorophyll-a between HT and LT) in period A  
519 (resp. 29%,  $\Delta\text{CHL}_{\text{total}} = 6.98 \text{ mg m}^{-2}$  in period B), indicating an overall enhancement of primary production.



a mis en forme: En-tête



521  
522 **Figure 10:** Comparison of mean chlorophyll-a profiles during HT and LT periods. The purple dashed lines represent the  
523 interquartile range (IQR) for LT periods, while the green dashed area represents the IQR for HT periods. The red regions indicate  
524 where the mean chlorophyll-a concentration during HT exceeds that during LT, and the blue regions indicate the opposite (LT >  
525 HT).  
526

a mis en forme: Police :+Titres CS (TimesNew Roman)

527 **Table 2:** Summary statistics of chlorophyll-a of four key parameters: maximum chlorophyll-a concentration, chlorophyll-a peak  
528 thickness, mean chlorophyll-a content, and the depth of the deep chlorophyll-a maximum during HT and LT periods.  
529

Period/features	Peak Thickness at 0.2 (mg m-3)			Depth of Max (m)		
	Mean	Median	STD	Mean	Median	STD
AHT	69.2	67.5	18.6	81.7	87	15.59
ALT	45.93	47	6.56	79.38	80.5	5.35

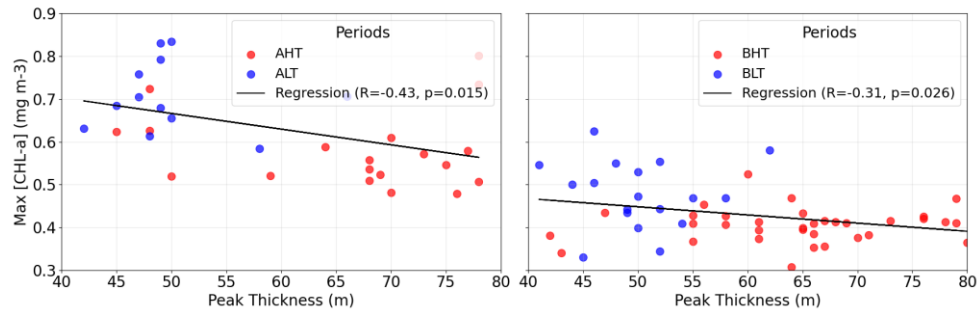
a mis en forme le tableau

a mis en forme: Police :+Titres CS (TimesNew Roman)

a mis en forme: Police :+Titres CS (TimesNew Roman)

a mis en forme: Police :+Titres CS (TimesNew Roman)

BHT	66.3	67	9.59	98.28	99.5	22.01
BLT	51	50.5	5.69	85.45	86.0	10.46
Period/features	<b>Max of chlorophyll-a</b> (mg m <sup>-3</sup> )			<b>Total Averaged Chlorophyll</b> (mg m <sup>-3</sup> )		
	Mean	Median	STD	Mean	Median	STD
AHT	0.60	0.58	0.09	36.28	34.69	6.36
ALT	0.72	0.71	0.07	31.84	31.73	2.09
BHT	0.43	0.41	0.11	31.36	30.77	3.91
BLT	0.47	0.47	0.09	24.38	24.21	7.02



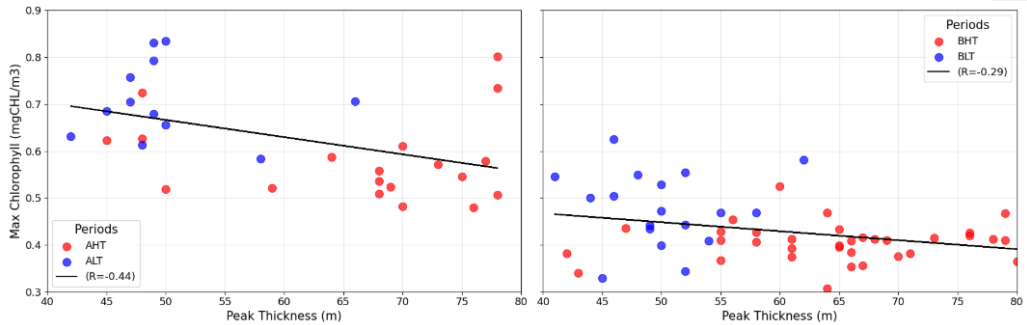


Figure 11: Relationship between Chlorophyll peak thickness (m) and maximum chlorophyll-a concentration (mg m-3) during HT and LT periods.

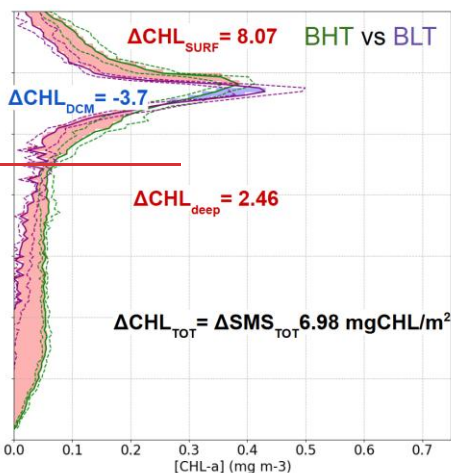
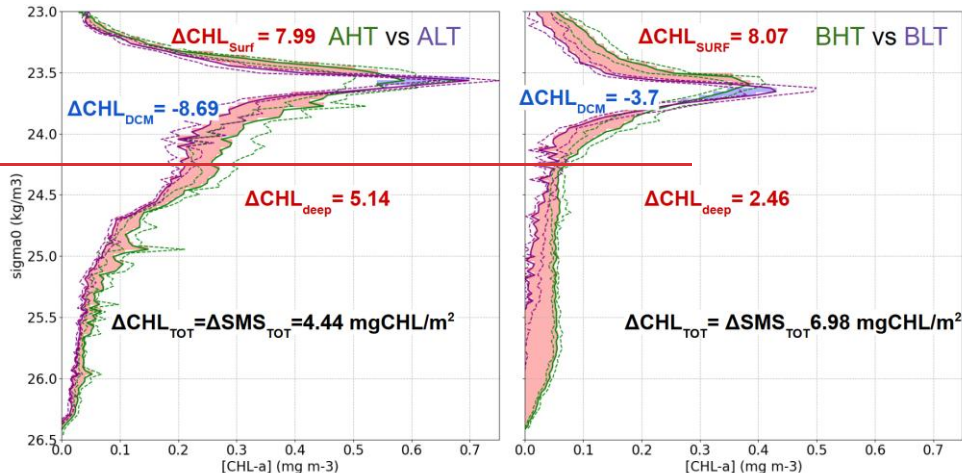
a mis en forme : Police :+Titres CS (TimesNew Roman)

#### Chlorophyll-a Diapycnal Redistribution

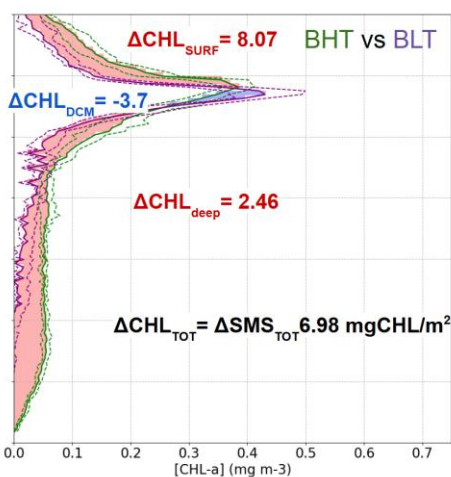
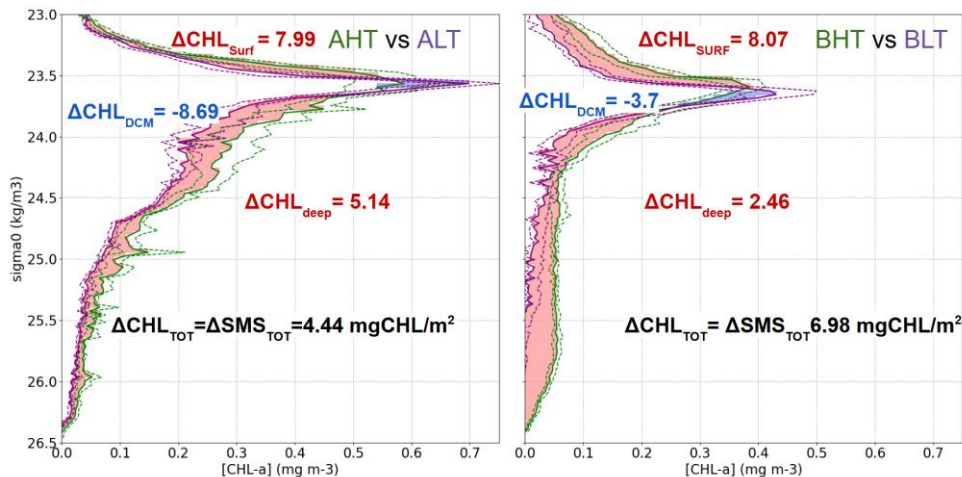
The net chlorophyll-a loss observed in the Deep chlorophyll-a Maximum (DCM) layer between low tide (LT) and high tide (HT) was estimated at  $\Delta\text{CHL}_{\text{DCM}} = -8.69 \text{ mg m}^{-2}$  or a 64% loss during period A ( $-3.7 \text{ mg m}^{-2}$  or 21% loss during period B) as shown in table 3. This depletion was redistributed both upward and downward across isopycnal layers.

The downward turbulent flux reaching the deep isopycnal layer ( $23.7 < \sigma_0 < 26.5$ ) was quantified as  $\Delta\text{CHL}_{\text{DEEP}} = 5.14 \text{ mg m}^{-2}$  in period A ( $2.46 \text{ mg m}^{-2}$  in period B). As this layer lay below the euphotic zone and did not support photosynthesis, biological consumption processes dominate ( $\Delta\text{SMS}_{\text{DEEP}} < 0$ ) implying that the observed chlorophyll-a increase represented a minimum estimate of the turbulent flux to depth  $\Delta\text{CHL}_{\text{DEEP}} \leq \Delta\text{Diff}_{\text{DEEP}}$  (eq.7). Thus, turbulent fluxes from the DCM supplied approximately 57% of the total chlorophyll-a increase observed in the deep layer. The turbulent flux toward the surface layer ( $\sigma_0 < 23.53$ ) was consequently estimated ~~as by mass conservation as~~  $\Delta\text{CHL}_{\text{DCM}} - \Delta\text{Diff}_{\text{DEEP}} = \Delta\text{Diff}_{\text{SURF}} = 3.55 \text{ mg m}^{-2}$  for period A ( $1.09 \text{ mg m}^{-2}$  for period B). Thus, turbulent fluxes from the DCM supplied approximately 38% of the total chlorophyll-a increase observed in the surface layer. The total variation in surface chlorophyll-a content between LT and HT reached  $7.99 \text{ mg m}^{-2}$  in period A ( $8.07 \text{ mg m}^{-2}$  in period B). After accounting for the turbulent input, the contribution of biological processes (production minus grazing) was calculated at  $\Delta\text{SMS}_{\text{surf}} = 4.55 \text{ mg m}^{-2}$  for period A ( $6.98 \text{ mg m}^{-2}$  for period B).

a mis en forme : Police :+Titres CS (TimesNew Roman)



552



553

Figure 12: Average vertical profiles of chlorophyll-a concentration ( $\text{mg m}^{-3}$ ) as a function of density ( $\sigma_0, \text{kg m}^{-3}$ ) for two regions: AHT vs ALT (left) and BHT vs BLT (right) based on density bins of 0.03. Shaded areas indicate differences in chlorophyll-a concentration between regimes, with red representing positive differences and blue indicating negative differences. Green and purple dashed areas represent the first and third quartiles for HT and LT periods.

a mis en forme: En-tête

558 Table 3 : Diapycnal statistics of integrated chlorophyll-a concentrations for each isopycnal layer

559

Layer	A				B			
	Period	Mean	Median	STD	Period	Mean	Median	STD
<b>Surface</b> <b>23.53</b> <b>(SURFACE)</b>	<b>AHT</b>	17.37	15.92	4.23	<b>BHT</b>	10.96	12.01	4.06
	<b>ALT</b>	9.38	9.56	1.10	<b>BLT</b>	2.89	3.04	1.95
<b>23.53 - 23.7</b> <b>(DCM)</b>	<b>AHT</b>	4.46	3.73	2.85	<b>BHT</b>	13.68	12.00	6.10
	<b>ALT</b>	13.15	13.7	2.04	<b>BLT</b>	17.38	17.38	3.32
<b>23.7 - 26.5</b> <b>(DEEP)</b>	<b>AHT</b>	14.45	13.07	3.77	<b>BHT</b>	6.57	6.23	1.43
	<b>ALT</b>	9.31	9.15	2.25	<b>BLT</b>	4.11	3.66	2.54

560

#### 561 4 Discussion

##### 562 AE1 as a mode water eddy

563 In this study, AE1 was identified as a mode-water eddy with an isopycnal structure distinct from that of classical anticyclonic  
564 eddies. While classical anticyclonic eddies typically feature depressed isopycnals that form a bowl-like shape restricting  
565 nutrient access to the euphotic zone, cyclonic eddies are characterized by domed isopycnals that enhance nutrient uplift. Mode-  
566 water eddies, a particular type of anticyclone, combine both doming and depression of isopycnals and have been reported as  
567 productive systems in subtropical regions (Chelton et al., 2011; McGillicuddy et al., 2007). In the case of AE1, ~~deeper, less~~  
568 ~~dense~~ isopycnals (~~at~~ around  $\sigma_0 \approx 23.5$ ) ~~showed~~ exhibited a doming ~~while~~ structure, whereas the upper, denser isopycnals  
569 (~~at~~ isopycnal at  $\sigma_0 \approx 23.7$ ) displayed a bowl-like depression shaped pattern (Figure 6). Notably, during period B, AE1 was less  
570 productive compared to other periods, which contrasts with McGillicuddy et al. (2007) (Figure 9). ~~This reduced~~ In  
571 McGillicuddy's framework, the doming part of an anticyclonic system can drive isopycnal uplift, potentially enhancing  
572 biological productivity ~~is likely~~ due to AE1's greater depth; although uplift of isopycnals was observed, their vertical

a mis en forme: a mis en forme le tableau

a mis en forme: Police :+Titres CS (TimesNew Roman)

a mis en forme: Police :+Titres CS (TimesNew Roman)

a mis en forme: Police :+Titres CS (TimesNew Roman)

a mis en forme: Police :+Titres CS (TimesNew Roman)

a mis en forme: Police :+Titres CS (TimesNew Roman)

a mis en forme: Police :+Titres CS (TimesNew Roman)

a mis en forme: Police :+Titres CS (TimesNew Roman)

a mis en forme: Police :+Titres CS (TimesNew Roman)

a mis en forme: Police :+Titres CS (TimesNew Roman)

a mis en forme: Police :+Titres CS (TimesNew Roman)

a mis en forme: Police :+Titres CS (TimesNew Roman)

a mis en forme: Police :+Titres CS (TimesNew Roman)

573 displacement remained insufficient to bring nutrients close to by injecting nutrient-rich waters into the euphotic layer zone.  
574 In our case, while such isopycnal uplift is indeed observed within AE1, the anticyclone core appears too deep for this  
575 mechanism to significantly increase productivity, likely because the uplifted. This finding suggests that the productivity of  
576 mode-water eddies or lense shaped eddies is strongly influenced by their vertical positioning depth. Consequently, the deep  
577 chlorophyll maximum (DCM) and likely the nutricline were situated deeper, limiting light availability and constraining  
578 photosynthetic activity.

579 *Dominance of ITs Over Near Inertial Waves*

580 One may ask whether wind forcing contributes significantly to the observed variability. Figure 13 shows a spectral analysis of  
581 the glider data over the whole period of acquisition (one month). A clear and intense peak is observed at 1e5 close enough to  
582 the M2 12.25 hours (fig8 and fig 13). At the inertial period (approximately 7 days at 2°–4°N), a small peak at 5e3 is found  
583 suggesting that the wind-driven processes like near-inertial waves are less important in our region.

584 These findings support the conclusion that internal tides are the dominant oscillation that explain the intensified mixing that  
585 we estimate at the time scale of the month.

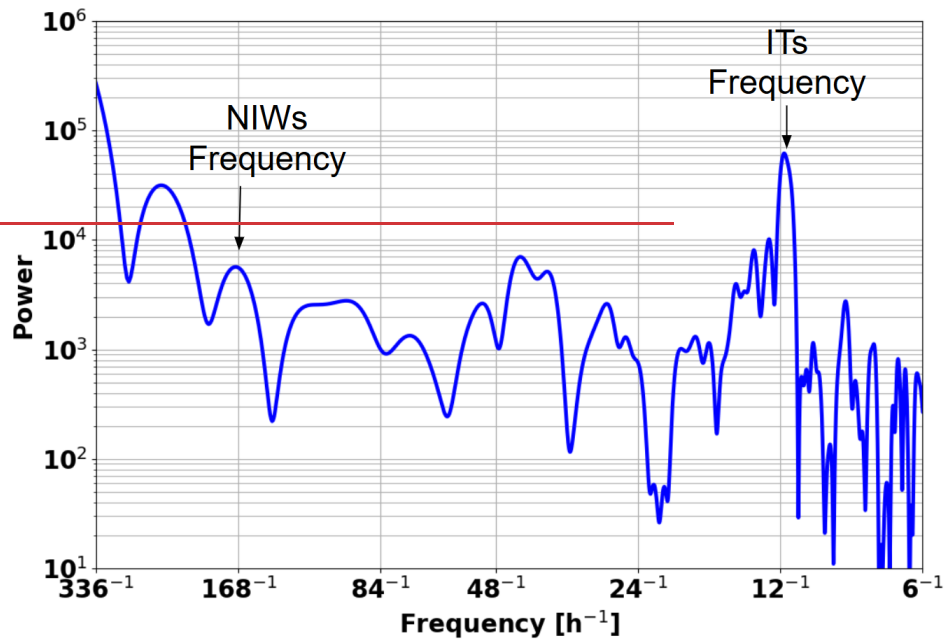
a mis en forme: En-tête

a mis en forme: Police :+Titres CS (TimesNew Roman)

a mis en forme: Police :+Titres CS (TimesNew Roman)

a mis en forme: Police :+Titres CS (TimesNew Roman)

a mis en forme: Police :+Titres CS (TimesNew Roman)



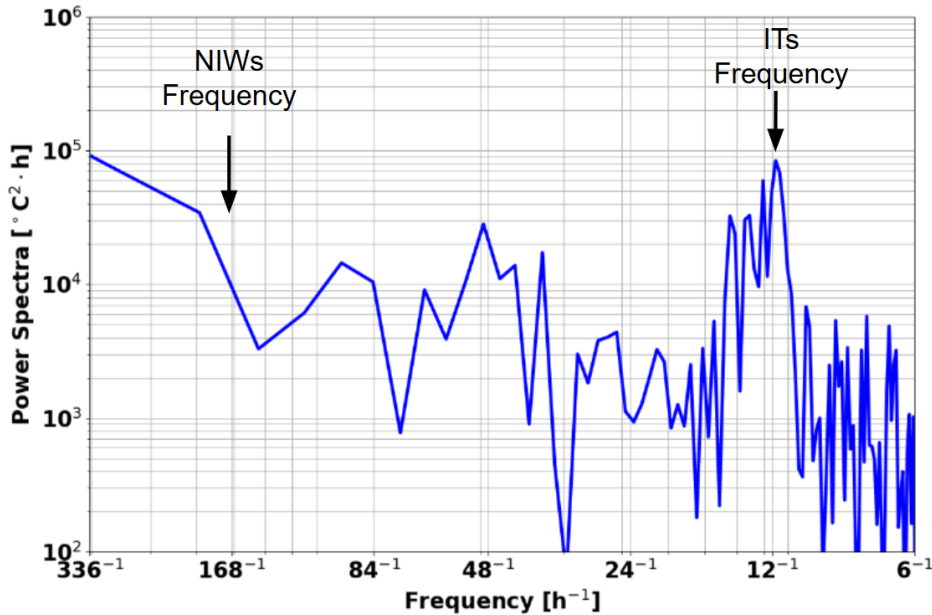


Figure 13: Spectral Analysis of temperature from the whole time series.

589 *Limits of Reversibility of LT and HT period and biological consequences*

590 *A key limitation of our study is the limited number of sampling periods available to effectively assess the impact of ITs (ITs)*  
 591 *on the vertical distribution of chlorophyll. This constraint not only reduces statistical robustness but also*

592 *An inherent challenge with glider-based measurements is the difficulty of separating spatial from temporal variability. Because*  
 593 *the glider moves continuously, the observed changes in hydrographic and biogeochemical properties combine true temporal*  
 594 *evolution at a fixed location with spatial gradients encountered along the track. In our study, the definition of four*  
 595 *hydrographically distinct regions (A, B, C, and D) was specifically designed to spatially isolate the observations. Within each*  
 596 *region, high-tide (HT) and low-tide (LT) phases were compared under similar water mass properties, thereby minimising the*  
 597 *influence of large-scale spatial gradients. Averaging over multiple tidal cycles within each region further reduced short-term*  
 598 *variability, providing a representative mean tidal signal.*  
 599 *Given that the deployment lasted only 26 days, our analysis primarily resolves variability on 1–3 day timescales associated*  
 600 *with internal tide activity, while higher-frequency (semi-diurnal, diurnal) signals are smoothed by daily averaging and lower-*

a mis en forme: En-tête

frequency (~15-day) spring-neap modulation is only partially captured. This means that we describe only part of the total internal tide impact, focusing on its short-term expression rather than the full fortnightly cycle. While this approach improves the robustness of our comparisons, the study remains constrained by the limited number of relevant intercomparison periods, which reduces statistical robustness and, restricts our ability to generalize the observed patterns. An additional and important nuance lies in the specific sequence in which high tide (HT) and low tide (LT) occur. In the available data for Period A, HT precedes LT (AHT/ALT), raising questions about the reversibility of tidal effects. The biological impact of HT followed by LT may differ significantly from a reversed sequence (ALT/AHT), particularly due to the lagged responses of phytoplankton communities.

This issue is especially relevant in our study region, which is characterized by regular and intense internal tide propagation, generating near-continuous alternation between HT and LT phases. Rather than isolating the direct effect of individual ITs, our approach focuses on a comparative analysis between HT and LT conditions, acknowledging the interconnectedness and cumulative nature of these processes. Notably, the LT phase may still harbour biological communities that have benefited from favourable mixing and nutrient supply conditions during the preceding HT phase. The extent to which this occurs depends on the response time of the resident phytoplankton taxa.

In oligotrophic tropical waters such as ours, phytoplankton communities are typically dominated by small-sized cells, including *Prochlorococcus*, *Synechococcus*, and various picoeukaryotes. These groups exhibit relatively rapid physiological responses to environmental changes, particularly to nutrient enrichment. For example, *Prochlorococcus* can respond to pulses of nitrogen or phosphorus within 12–36 hours (Moore et al., 2007; Partensky et al., 1999), while *Synechococcus* and picoeukaryotes tend to show measurable increases in biomass within 24–72 hours (Calvo-Díaz et al., 2008; Fuchs et al., 2023; Scanlan et al., 2009; Zubkov et al., 2000). In contrast, larger phytoplankton such as diatoms are less competitive under nutrient-poor conditions and typically require more sustained or intense inputs to initiate growth, with response times ranging from 2 to 4 days (Falkowski et al., 1998; Marañón et al., 2000). In our region, assuming that the biological response occurs within approximately one day, this factor is unlikely to significantly influence our results. Consequently, the AHT/ALT sequence would yield similar outcomes to an ALT/AHT sequence. The cumulative evidence from our findings (Fig. 9 and Fig. 11) supports this hypothesis, suggesting that the phytoplankton species in our region exhibit a rapid response to light and nutrient availability. Further validation of this hypothesis will be achieved through complementary analysis of AMAZOMIX cytometry data in future studies.

#### 628 *Chlorophyll turbulent vertical fluxes*

629 The diapycnal redistribution of chlorophyll-a observed between high tide (HT) and low tide (LT) phases (Fig. 12) is attributed  
630 to mixing driven by internal tides (IT), under the assumption that large-scale background conditions remain similar between  
631 HT and LT subperiods within the same overall period. Additionally, we argue that ITs dominate over near-inertial waves

a mis en forme: Police :+Titres CS (TimesNewRoman)

a mis en forme: Police :+Titres CS (TimesNewRoman)

632 (NIWs) in transporting biomass both upward into the euphotic zone and downward into deeper layers. This assumption holds  
633 only if the water masses and active processes are comparable between the two phases. We verified that the water masses were  
634 sufficiently similar to support this, but we acknowledge that this approach neglects possible contributions from other vertical  
635 mixing processes, such as NIWs or frontal activity, which may differ between HT and LT. Longer time series would help  
636 quantify these fluxes more precisely, beyond the limitations of a single-event analysis.

637 The deep chlorophyll maximum (DCM), located at the interface between nutrient-rich deep waters and the light-limited upper  
638 layers (Ma et al. (Ma et al., 2023) [ma](#)), showed a net biomass loss between HT and LT, with 21% (period B) to over 60%  
639 (period A) exported downward and the remainder redistributed upward. These findings partly align with the observations of  
640 Gaxiola-Castro et al. (2002), who reported internal wave-driven upward transport of chlorophyll in the Gulf of California,  
641 increasing surface biomass by around 40% during spring tides — consistent with the increases we observe. However, their  
642 study did not quantify the downward flux, which in our case accounts for nearly half of the deep-layer biomass (~57%).

643 This redistribution has important implications for the trophic network. As Durham and Stocker (2012) have shown, thin  
644 phytoplankton layers act as trophic hotspots, intensifying interactions among phytoplankton, zooplankton, and higher trophic  
645 levels. The downward export of biomass not only contributes to the biological carbon pump but also reduces resource  
646 availability for mesopelagic organisms. Meanwhile, the upward transfer enhances primary production, increasing surface  
647 biomass by 14–29% and reinforcing upper trophic chains. Overall, these results highlight the crucial role of internal tides in  
648 shaping marine trophic dynamics and underscore the importance of accounting for both upward and downward turbulent  
649 fluxes.

## 650 5 Conclusion

651 This study provides new insights into the role of internal tides (ITs) in reshaping and homogenizing the vertical distribution of  
652 chlorophyll-a and enhancing primary productivity off the Amazon shelf. Using a combination of satellite observations and  
653 high-resolution glider data from the AMAZOMIX 2021 campaign, we show that ITs are key drivers of short-term vertical  
654 chlorophyll variability.

655 The region is marked by dynamic interactions between major current systems, including the North Brazil Current (NBC), the  
656 NBC retroflection, and the North Equatorial Countercurrent (NECC), as well as the presence of mesoscale and submesoscale  
657 structures. During the glider deployment, five internal solitary wave (ISW) signals and a large anticyclonic eddy (AE1) were  
658 detected by remote sensing. Combined with glider data, observations showed that AE1 locally reduced productivity by limiting  
659 exchanges between surface and deep nutrient-rich layers.

660 Glider profiles revealed strong vertical isopycnal oscillations between 15 and 45 meters at semi-diurnal tidal frequencies. The  
661 intensity of these oscillations allowed us to separate periods of strong internal tide activity (high tide, HT) from periods of

662 weaker activity (low tide, LT), which, under similar water mass conditions, provided a robust basis for comparing the effect  
663 of internal tides on chlorophyll-a. Importantly, while ocean colour satellites are unable to resolve such fine-scale diurnal  
664 variations, the glider was able to capture these dynamics, offering unique insights into the vertical redistribution of chlorophyll-  
665 a.

666 Our results show that ITs redistribute chlorophyll-a vertically. This results in a thickening of the deep chlorophyll maximum  
667 (DCM), increasing by 30–50% (~+15 m) during high-tide periods, and a reduction in its peak chlorophyll-a concentration by  
668 9–17% (~−0.1 mg m<sup>-3</sup>). These effects are the results of both advection and mixing of the ITs.

669 First, the advection of the ITs induce vertical motion of the DCM, following the associated isopycnal displacement, which,  
670 when averaged results in a larger DCM peak and combined with light conditions, may enhance primary production since the  
671 light gradient is not linear with depth. Indeed, in the uplift condition, chlorophyll receives more light and increased Primary  
672 production is expected; an uplift exposes the chlorophyll-a to light gain than the light loss caused by a downlift.

673 Second, the mixing plays a major role in reshaping the chlorophyll. Turbulent transport redistributes chlorophyll-a both upward  
674 into the euphotic surface layers (accounting for ~40% of the chlorophyll content above the DCM) and downward into the  
675 aphotic deep layers (about ~60% of the chlorophyll content below the DCM), with these fluxes originating from the DCM  
676 pool and leading to losses of up to 65%.

677 In overall, the combined effect of advection and mixing, by improving both light availability and nutrient supply, leads to an  
678 increase in the total chlorophyll-a content integrated over the whole water column by 14–29% during high internal tide phases  
679 compared to low tide phases.

680 For future research, we recommend a more systematic use of gliders in oceanographic campaigns to enhance our understanding  
681 of internal tides and their interactions with ocean biogeochemistry. We strongly advocate for the combined integration of  
682 biological, physical, and turbulence sensors to better characterize the small-scale processes that control phytoplankton  
683 dynamics and primary production.

684

#### 685 **Data availability**

686 The AMAZOMIX glider data are available upon request by contacting the corresponding author.

687 Sentinel-1 SAR imagery: Copernicus Open Access Hub – <https://scihub.copernicus.eu/dhus/>

688 MODIS-TERRA/AQUA imagery: NASA Earthdata – <https://earthdata.nasa.gov/>

689 Chlorophyll-a and euphotic depth (Zeu): GlobColour via Copernicus Marine Service –

690 <https://resources.marine.copernicus.eu/products>  
 691 Absolute Dynamic Topography and geostrophic velocities: Copernicus Marine Service (SSALTO/DUACS)  
 692 [https://data.marine.copernicus.eu/product/SEALEVEL\\_GLO\\_PHY\\_MDT\\_008\\_063/description](https://data.marine.copernicus.eu/product/SEALEVEL_GLO_PHY_MDT_008_063/description)  
 693 Bathymetry data: NOAA CoastWatch Data Portal – <https://coastwatch.pfeg.noaa.gov/>

694 **Authors contributions**

695  
 696 AKL: funding acquisition. AM and AKL, with assistance from ID,VP,ACS,AB,MA: conceptualization and  
 697 methodology. AM, with assistance from AB: data pre-processing. Formal analysis: AM with interactions from  
 698 all co-authors. Preparation of the manuscript: AM with contributions from all co-authors. This work is a  
 699 contribution to the LMI TAPIOCA ([www.tapioca.ird.fr](http://www.tapioca.ird.fr)).

700 **Acknowledgements**  
 701  
 702 M.A. thanks the support of the Brazilian research Network on Global Climate Change - Rede CLIMA (FINEP-CNPq 439  
 703 437167/2016-0)  
 704  
 705 The authors would like to thank the “Flotte Océanographique Française” and the officers and crew of the R/V  
 706 Antea for their contribution to the success of the operations aboard the R/V ANTEA, as well as, all the scientists  
 707 involved in data and water samples collection, for their valuable support during and after the AMAZOMIX cruise.  
 708 We acknowledge the Brazilian authorities for authorising the survey, the National french parc of instrument (DT-  
 709 INSU) for their instrument during the cruise and support in data analysis, as well as, the US-IMAGO from IRD for  
 710 its help during the cruise and for biogeochemical data analysis.

711 **Financial support**  
 712 This work is a part of the project “AMAZOMIX”, funded multiple agencies : the “Flotte Océanographique  
 713 Française” that funded the 40 days at sea of the R/V Antea, the Institut de Recherche pour le Développement (IRD),  
 714 via among other the LMI TAPIOCA, the CNES, within the framework of the APR TOSCA MIAMAZ TOSCA  
 715 project (PIs Ariane Koch-Larrouy, Vincent Vantrepotte, and Isabelle Dadou), the LEGOS and the program  
 716 international Franco-Brazileiro GUYAMAZON (call No 005/2017). It is also part of the PhD Thesis of Amine  
 717 M’hamdi, funded by the Fundação de Amparo a Ciência e Tecnologia do Estado de Pernambuco (FACEPE), under  
 718 the co-advisement of Ariane Koch-Larrouy, Alex Costa da Silva, Isabelle Dadou and Vincent Vantrepotte.

719 **Competing interests**  
 720 The authors declare that they have no conflict of interest.  
 721

722 **References**

723 Aguedjou, H.M.A., Dadou, I., Chaigneau, A., Morel, Y., Alory, G., 2019. Eddies in the Tropical Atlantic Ocean and Their  
 724 Seasonal Variability. *Geophys. Res. Lett.* 46, 12156–12164. <https://doi.org/10.1029/2019GL083925>

725 Alford, M.H., Peacock, T., MacKinnon, J.A., Nash, J.D., Buijsman, M.C., Centurioni, L.R., Chao, S.-Y., Chang, M.-H.,  
 726 Farmer, D.M., Fringer, O.B., 2015. The formation and fate of internal waves in the South China Sea. *Nature* 521,  
 727 65–69.

728 Assene, F., Koch-Larrouy, A., Dadou, I., Tchilibou, M., Morvan, G., Chanut, J., Costa da Silva, A., Vantrepotte, V., Allain,  
 729 D., Tran, T.-K., 2024. Internal tides off the Amazon shelf—Part 1: The importance of the structuring of ocean  
 730 temperature during two contrasted seasons. *Ocean Sci.* 20, 43–67.

731 Baines, P.G., 1982. On internal tide generation models. *Deep Sea Res. Part Oceanogr. Res. Pap.* 29, 307–338.

732 Beardsley, R.C., Candela, J., Limeburner, R., Geyer, W.R., Lentz, S.J., Castro, B.M., Cacchione, D., Cameiro, N., 1995. The  
 733 M<sub>2</sub> tide on the Amazon Shelf. *J. Geophys. Res. Oceans* 100, 2283–2319. <https://doi.org/10.1029/94JC01688>

734 Bourgault, D., Hamel, C., Cyr, F., Tremblay, J.-É., Galbraith, P.S., Dumont, D., Gratton, Y., 2011. Turbulent nitrate fluxes  
 735 in the Amundsen Gulf during ice-covered conditions. *Geophys. Res. Lett.* 38, 2011GL047936.  
 736 <https://doi.org/10.1029/2011GL047936>

737 Brandt, P., Rubino, A., Fischer, J., 2002. Large-Amplitude Internal Solitary Waves in the North Equatorial Countercurrent. *J.  
 738 Phys. Oceanogr.* 32, 1567–1573. [https://doi.org/10.1175/1520-0485\(2002\)032<1567:LAISWI>2.0.CO;2](https://doi.org/10.1175/1520-0485(2002)032<1567:LAISWI>2.0.CO;2)

739 Calvo-Díaz, A., Morán, X.A.G., Suárez, L.Á., 2008. Seasonality of picophytoplankton chlorophyll a and biomass in the  
 740 central Cantabrian Sea, southern Bay of Biscay. *J. Mar. Syst.* 72, 271–281.

741 Capuano, T.A., Koch-Larrouy, A., Nugroho, D., Zaron, E., Dadou, I., Tran, K., Vantrepotte, V., Allain, D., 2025. Impact of  
 742 Internal Tides on Distributions and Variability of Chlorophyll-a and Nutrients in the Indonesian Seas. *J. Geophys.  
 743 Res. Oceans* 130, e2022JC019128. <https://doi.org/10.1029/2022JC019128>

744 Chaigneau, A., Eldin, G., Dewitte, B., 2009. Eddy activity in the four major upwelling systems from satellite altimetry  
 745 (1992–2007). *Prog. Oceanogr.* 83, 117–123.

746 Chaigneau, A., Gizolme, A., Grados, C., 2008. Mesoscale eddies off Peru in altimeter records: Identification algorithms and  
 747 eddy spatio-temporal patterns. *Prog. Oceanogr.* 79, 106–119.

748 De Macedo, C.R., Koch-Larrouy, A., Da Silva, J.C.B., Magalhães, J.M., Lentini, C.A.D., Tran, T.K., Rosa, M.C.B.,  
 749 Vantrepotte, V., 2023. Spatial and temporal variability in mode-1 and mode-2 internal solitary waves from MODIS-  
 750 Terra sun glint off the Amazon shelf. *Ocean Sci.* 19, 1357–1374.

751 Egbert, G.D., Ray, R.D., 2001. Estimates of M<sub>2</sub> tidal energy dissipation from TOPEX/Poseidon altimeter data. *J. Geophys.  
 752 Res. Oceans* 106, 22475–22502. <https://doi.org/10.1029/2000JC000699>

753 Falkowski, P.G., Barber, R.T., Smetacek, V., 1998. Biogeochemical Controls and Feedbacks on Ocean Primary Production.  
 754 *Science* 281, 200–206. <https://doi.org/10.1126/science.281.5374.200>

755 Falkowski, P.G., Knoll, A.H., 2007. An introduction to primary producers in the sea: who they are, what they do, and when  
 756 they evolved, in: *Evolution of Primary Producers in the Sea*. Elsevier, pp. 1–6.

757 Fratantoni, D.M., Glickson, D.A., 2002. North Brazil Current ring generation and evolution observed with SeaWiFS. *J. Phys.  
 758 Oceanogr.* 32, 1058–1074.

759 Franks, P.J.S., 2002. NPZ Models of Plankton Dynamics: Their Construction, Coupling to Physics, and Application. *J.  
 760 Oceanogr.* 58, 379–387. <https://doi.org/10.1023/A:1015874028196>

761 Fuchs, R., Rossi, V., Caille, C., Bensoussan, N., Pinazo, C., Grosso, O., Thyssen, M., 2023. Intermittent Upwelling Events  
 762 Trigger Delayed, Major, and Reproducible Pico-Nanophytoplankton Responses in Coastal Oligotrophic Waters.  
 763 *Geophys. Res. Lett.* 50, e2022GL102651. <https://doi.org/10.1029/2022GL102651>

764 Gabiou, M., Vinzon, S.B., Paiva, A.M., 2005. Tidal propagation over fluid mud layers on the Amazon shelf. *Cont. Shelf  
 765 Res.* 25, 113–125.

766 Garau, B., Ruiz, S., Zhang, W.G., Pascual, A., Heslop, E., Kerfoot, J., Tintoré, J., 2011. Thermal Lag Correction on Slocum  
 767 CTD Glider Data. *J. Atmospheric Ocean. Technol.* 28, 1065–1071. <https://doi.org/10.1175/JTECH-D-10-05030.1>

768 Garnesson, P., Mangin, A., Fanton d'Andon, O., Demaria, J., Bretagnon, M., 2019. The CMEMS GlobColour chlorophyll  
 769 &lt;&gt; a &lt;&gt; product based on satellite observation: multi-sensor merging and flagging strategies. *Ocean  
 770 Sci.* 15, 819–830. <https://doi.org/10.5194/os-15-819-2019>

771 Garzoli, S.L., Field, A., Yao, Q., 2003. North Brazil Current rings and the variability in the latitude of retroflection, in:  
 772 Elsevier Oceanography Series. Elsevier, pp. 357–373.

773 Gaxiola-Castro, G., Álvarez-Borrego, S., Nájera-Martínez, S., Zirino, A., 2002. Internal waves effect on the Gulf of  
 774 California phytoplankton. *Cienc. Mar.* 28, 297–309. <https://doi.org/10.7773/cm.v28i3.222>

775 Geyer, W.R., 1995. Tide-induced mixing in the Amazon Frontal Zone. *J. Geophys. Res. Oceans* 100, 2341–2353.  
 https://doi.org/10.1029/94JC02543

776 Gohin, F., 2011. Annual cycles of chlorophyll-a, non-algal suspended particulate matter, and turbidity observed from space  
 777 and in-situ in coastal waters. *Ocean Sci.* 7, 705–732.

778 Grimshaw, R., 2003. Internal Solitary Waves, in: Grimshaw, R. (Ed.), *Environmental Stratified Flows, Topics in  
 779 Environmental Fluid Mechanics*. Kluwer Academic Publishers, Boston, pp. 1–27. [https://doi.org/10.1007/0-306-48024-7\\_1](https://doi.org/10.1007/0-306-48024-7_1)

780 Grisouard, N., Staquet, C., Gerkema, T., 2011. Generation of internal solitary waves in a pycnocline by an internal wave  
 781 beam: a numerical study. *J. Fluid Mech.* 676, 491–513.

782 Holligan, P.M., Pingree, R.D., Mardell, G.T., 1985. Oceanic solitons, nutrient pulses and phytoplankton growth. *Nature* 314,  
 783 348–350.

784 Holloway, G., Denman, K., 1989. Influence of internal waves on primary production. *J. Plankton Res.* 11, 409–413.

785 Horne, E.P., Loder, J.W., Naime, C.E., Oakey, N.S., 1996. Turbulence dissipation rates and nitrate supply in the upper water  
 786 column on Georges Bank. *Deep Sea Res. Part II Top. Stud. Oceanogr.* 43, 1683–1712.

787 Hu, C., Feng, L., Lee, Z., Davis, C.O., Mannino, A., McClain, C.R., Franz, B.A., 2012. Dynamic range and sensitivity  
 788 requirements of satellite ocean color sensors: learning from the past. *Appl. Opt.* 51, 6045–6062.

789 Ivanov, V.A., Ivanov, L.I., Lisichenok, A.D., 1990. Redistribution of energy of the internal tidal wave in the North  
 790 Equatorial Countercurrent region. *Sov. J. Phys. Oceanogr.* 1, 383–386.

791 Jackson, Christopher.R., Alpers, W., 2010. The role of the critical angle in brightness reversals on sunglint images of the sea  
 792 surface. *J. Geophys. Res. Oceans* 115, 2009JC006037. <https://doi.org/10.1029/2009JC006037>

793 Jackson, C.R., Da Silva, J.C., Jeans, G., 2012. The generation of nonlinear internal waves. *Oceanography* 25, 108–123.

794 Jacobsen, J.R., Edwards, C.A., Powell, B.S., Colosi, J.A., Fiechter, J., 2023. Nutricline adjustment by internal tidal beam  
 795 generation enhances primary production in idealized numerical models. *Front. Mar. Sci.* 10, 1309011.

796 Jeans, D.R.G., Sherwin, T.J., 2001. The variability of strongly non-linear solitary internal waves observed during an  
 797 upwelling season on the Portuguese shelf. *Cont. Shelf Res.* 21, 1855–1878.

798 Johns, W.E., Lee, T.N., Beardsley, R.C., Candel, J., Limeburner, R., Castro, B., 1998. Annual cycle and variability of the  
 799 North Brazil Current. *J. Phys. Oceanogr.* 28, 103–128.

800 Kahru, M., 1983. Phytoplankton patchiness generated by long internal waves: A model. *Mar. Ecol. Prog. Ser.* Oldendorf 10,  
 801 111–117.

802 Kaneko, H., Tanaka, T., Wakita, M., Sasaki, K., Okunishi, T., Miyazawa, Y., Zhang, R., Tatamisashi, S., Sato, Y.,  
 803 Hashimukai, T., 2025. Topographically driven vigorous vertical mixing supports mesoscale biological production in  
 804 the Tsugaru Gyre. *Nat. Commun.* 16, 3656.

805 Kantha, L.H., Tierney, C.C., 1997. Global baroclinic tides. *Prog. Oceanogr.* 40, 163–178.

806 Koch-Larrouy, A., Lengaigne, M., Terray, P., Madec, G., Masson, S., 2010. Tidal mixing in the Indonesian Seas and its  
 807 effect on the tropical climate system. *Clim. Dyn.* 34, 891–904.

808 Krahmann, G., 2023. GEOMAR FB1-PO Matlab Slocum glider processing toolbox.

809 Kunze, E., 2017. Internal-wave-driven mixing: Global geography and budgets. *J. Phys. Oceanogr.* 47, 1325–1345.

810 Lamb, K.G., Xiao, W., 2014. Internal solitary waves shoaling onto a shelf: Comparisons of weakly-nonlinear and fully  
 811 nonlinear models for hyperbolic-tangent stratifications. *Ocean Model.* 78, 17–34.

812 Lande, R., Yentsch, C.S., 1988. Internal waves, primary production and the compensation depth of marine phytoplankton. *J.  
 813 Plankton Res.* 10, 565–571.

814 Law, C.S., Abraham, E.R., Watson, A.J., Liddicoat, M.I., 2003. Vertical eddy diffusion and nutrient supply to the surface  
 815 mixed layer of the Antarctic Circumpolar Current. *J. Geophys. Res. Oceans* 108, 2002JC001604.  
 https://doi.org/10.1029/2002JC001604

816 Lewis, M.R., Hebert, D., Harrison, W.G., Platt, T., Oakey, N.S., 1986. Vertical Nitrate Fluxes in the Oligotrophic Ocean.  
 817 *Science* 234, 870–873. <https://doi.org/10.1126/science.234.4778.870>

818 Liu, C., Pinkel, R., Klymak, J., Hsu, M., Chen, H., Villanoy, C., 2006. Nonlinear internal waves from the Luzon Strait. *Eos  
 819 Trans. Am. Geophys. Union* 87, 449–451. <https://doi.org/10.1029/2006EO420002>

a mis en forme : En-tête

a mis en forme : Police :+Titres CS (TimesNew Roman), Non Gras

a mis en forme : Police :+Titres CS (TimesNew Roman)

823 Lyard, F.H., Allain, D.J., Cancet, M., Carrère, L., Picot, N., 2021. FES2014 global ocean tide atlas: design and performance. Ocean Sci. 17, 615–649.

824 Kouogang, F., Koch-Larrouy, A., Magalhaes, J., Costa da Silva, A., Kerhervé, D., Bertrand, A., Cervelli, E., Assene, F.,

825 Temon, J.-F., Rousselot, P., 2025.

826

827 Ma, L., Bai, X., Laws, E.A., Xiao, W., Guo, C., Liu, X., Chiang, K., Gao, K., Huang, B., 2023. Responses of Phytoplankton Communities to Internal Waves in Oligotrophic Oceans. J. Geophys. Res. Oceans 128, e2023JC020201. <https://doi.org/10.1029/2023JC020201>

828 Magalhaes, J.M., da Silva, J.C.B., Buijsman, M.C., Garcia, C.A.E., 2016. Effect of the North Equatorial Counter Current on the generation and propagation of internal solitary waves off the Amazon shelf (SAR observations). Ocean Sci. 12, 243–255. <https://doi.org/10.5194/os-12-243-2016>

829 Mahadevan, A., Campbell, J.W., 2002. Biogeochemical patchiness at the sea surface. Geophys. Res. Lett. 29. <https://doi.org/10.1029/2001GL014116>

830 Marañón, E., Holligan, P.M., Varela, M., Mouríño, B., Bale, A.J., 2000. Basin-scale variability of phytoplankton biomass, production and growth in the Atlantic Ocean. Deep Sea Res. Part Oceanogr. Res. Pap. 47, 825–857.

831 Martin, A.P., Lucas, M.I., Painter, S.C., Pidcock, R., Prandke, Hartmut, Prandke, Holger, Stinchcombe, M.C., 2010. The supply of nutrients due to vertical turbulent mixing: A study at the Porcupine Abyssal Plain study site in the northeast Atlantic. Deep Sea Res. Part II Top. Stud. Oceanogr. 57, 1293–1302.

832 McDougall, T.J., Barker, P.M., 2011. Getting started with TEOS-10 and the Gibbs Seawater (GSW) oceanographic toolbox. Scoriapsò WG 127, 1–28.

833 McInerney, J.B.T., Forrest, A.L., Schladow, S.G., Largier, J.L., 2019. How to Fly an Autonomous Underwater Glider to Measure an Internal Wave, in: OCEANS 2019 MTS/IEEE SEATTLE. Presented at the OCEANS 2019 MTS/IEEE SEATTLE, IEEE, Seattle, WA, USA, pp. 1–8. <https://doi.org/10.23919/OCEANS40490.2019.8962407>

834 Mikaelyan, A.S., Zatsepin, A.G., Kubryakov, A.A., 2020. Effect of mesoscale eddy dynamics on bioproductivity of the marine ecosystems. Phys. Oceanogr. 27, 590–618.

835 Moore, C.M., Seeaye, S., Hickman, A.E., Allen, J.T., Lucas, M.I., Planquette, H., Pollard, R.T., Poulton, A.J., 2007. Iron-light interactions during the CROZet natural iron bloom and Export experiment (CROZEX) I: Phytoplankton growth and photophysiology. Deep Sea Res. Part II Top. Stud. Oceanogr. 54, 2045–2065.

836 Morel, A., 1988. Optical modeling of the upper ocean in relation to its biogenous matter content (case I waters). J. Geophys. Res. Oceans 93, 10749–10768. <https://doi.org/10.1029/JC093C09p10749>

837 Moum, J.N., Farmer, D.M., Smyth, W.D., Armi, L., Vagle, S., 2003. Structure and generation of turbulence at interfaces strained by internal solitary waves propagating shoreward over the continental shelf. J. Phys. Oceanogr. 33, 2093–2112.

838 Munk, W., Wunsch, C., 1998. Abyssal recipes II: energetics of tidal and wind mixing. Deep Sea Res. Part Oceanogr. Res. Pap. 45, 1977–2010. [https://doi.org/10.1016/S0967-0637\(98\)00070-3](https://doi.org/10.1016/S0967-0637(98)00070-3)

839 Nash, J.D., Kunze, E., Toole, J.M., Schmitt, R.W., 2004. Internal tide reflection and turbulent mixing on the continental slope. J. Phys. Oceanogr. 34, 1117–1134.

840 Neto, A.V.N., Da Silva, A.C., 2014. Seawater temperature changes associated with the North Brazil current dynamics. Ocean Dyn. 64, 13–27.

841 Partensky, F., Hess, W.R., Vaultot, D., 1999. *Prochlorococcus*, a Marine Photosynthetic Prokaryote of Global Significance. Microbiol. Mol. Biol. Rev. 63, 106–127. <https://doi.org/10.1128/MMBR.63.1.106-127.1999>

842 Pegliasco, C., Chaigneau, A., Morrow, R., 2015. Main eddy vertical structures observed in the four major Eastern Boundary Upwelling Systems. J. Geophys. Res. Oceans 120, 6008–6033. <https://doi.org/10.1002/2015JC010950>

843 Pujol, M.-I., Faugère, Y., Taburet, G., Dupuy, S., Pelloquin, C., Ablain, M., Picot, N., 2016. DUACS DT2014: the new multi-mission altimeter data set reprocessed over 20years. Ocean Sci. 12, 1067–1090. <https://doi.org/10.5194/os-12-1067-2016>

844 Ruault, V., Jouanno, J., Durand, F., Chanut, J., Benshila, R., 2020. Role of the Tide on the Structure of the Amazon Plume: A Numerical Modeling Approach. J. Geophys. Res. Oceans 125, e2019JC015495. <https://doi.org/10.1029/2019JC015495>

845 Sangrà, P., Martínez, A., Lubián, L., Antoranz, A., Rodríguez Santana, A., Rodríguez, S., Sobrino, C., Pelegrí, J.L.,

873 Hernández Guerra, A., 2002. Mesoscale Structures and Chlorophyll Distribution In The Bransfield Strait (antarctica),  
 874 in: EGS General Assembly Conference Abstracts. p. 3312.

875 Scanlan, D.J., Ostrowski, M., Mazard, S., Dufresne, A., Garczarek, L., Hess, W.R., Post, A.F., Hagemann, M., Paulsen, I.,  
 876 Partensky, F., 2009. Ecological Genomics of Marine Picocyanobacteria. *Microbiol. Mol. Biol. Rev.* 73, 249–299.  
 877 <https://doi.org/10.1128/MMBR.00035-08>

878 Schott, F.A., Fischer, J., Stramma, L., 1998. Transports and pathways of the upper-layer circulation in the western tropical  
 879 Atlantic. *J. Phys. Oceanogr.* 28, 1904–1928.

880 Silva, A., Araujo, M., Medeiros, C., Silva, M., Bourles, B., 2005. Seasonal changes in the mixed and barrier layers in the  
 881 western Equatorial Atlantic. *Braz. J. Oceanogr.* 53, 83–98. <https://doi.org/10.1590/S1679-87592005000200001>

882 Silva, A.C., Bourlès, B., Araujo, M., 2009. Circulation of the thermocline salinity maximum waters off the Northern Brazil  
 883 as inferred from in situ measurements and numerical results, in: *Annales Geophysicae*. Copernicus GmbH, pp.  
 884 1861–1873.

885 Sprintall, J., Gordon, A.L., Koch-Larrouy, A., Lee, T., Potemra, J.T., Pujiana, K., Wijffels, S.E., 2014. The Indonesian seas  
 886 and their role in the coupled ocean–climate system. *Nat. Geosci.* 7, 487–492.

887 Tchilibou, M., Koch-Larrouy, A., Barbot, S., Lyard, F., Morel, Y., Jouanno, J., Morrow, R., 2022. Internal tides off the  
 888 Amazon shelf during two contrasted seasons: interactions with background circulation and SSH imprints. *Ocean  
 889 Sci.* 18, 1591–1618. <https://doi.org/10.5194/os-18-1591-2022>

890 Testor, P., de Young, B., Rudnick, D.L., Glenn, S., Hayes, D., Lee, C.M., Pattiariatchi, C., Hill, K., Heslop, E., Turpin, V.,  
 891 Alenius, P., Barrera, C., Barth, J.A., Beaird, N., Béchu, G., Bosse, A., Bourrin, F., Brearley, J.A., Chao, Y., Chen, S.,  
 892 Chiggiato, J., Coppola, L., Crout, R., Cummings, J., Curry, B., Curry, R., Davis, R., Desai, K., DiMarco, S.,  
 893 Edwards, C., Fielding, S., Fer, I., Frajka-Williams, E., Gildor, H., Goni, G., Gutierrez, D., Haugan, P., Hebert, D.,  
 894 Heiderich, J., Henson, S., Heywood, K., Hogan, P., Houpt, L., Huh, S., Inall, M., Ishii, M., Ito, S., Itoh, S., Jan, S.,  
 895 Kaiser, J., Karstensen, J., Kirkpatrick, B., Klymak, J., Kohut, J., Krahmann, G., Krug, M., McClatchie, S.,  
 896 Marin, F., Mauri, E., Mehra, A., P. Meredith, M., Meunier, T., Miles, T., Morell, J.M., Mortier, L., Nicholson, S.,  
 897 O'Callaghan, J., O'Conchubhair, D., Oke, P., Pallás-Sanz, E., Palmer, M., Park, J., Perivoliotis, L., Poulain, P.-M.,  
 898 Perry, R., Queste, B., Rainville, L., Rehm, E., Roughan, M., Rome, N., Ross, T., Ruiz, S., Saba, G., Schaeffer, A.,  
 899 Schönhau, M., Schroeder, K., Shimizu, Y., Sloyan, B.M., Smeed, D., Snowden, D., Song, Y., Swart, S., Tenreiro,  
 900 M., Thompson, A., Tintore, J., Todd, R.E., Toro, C., Venables, H., Wagawa, T., Waterman, S., Watlington, R.A.,  
 901 Wilson, D., 2019. OceanGliders: A Component of the Integrated GOOS. *Front. Mar. Sci.* 6, 422.  
 902 <https://doi.org/10.3389/fmars.2019.00422>

903 Thomalla, S.J., Moutier, W., Ryan-Keogh, T.J., Gregor, L., Schütt, J., 2018. An optimized method for correcting  
 904 fluorescence quenching using optical backscattering on autonomous platforms. *Limnol. Oceanogr. Methods* 16,  
 905 132–144. <https://doi.org/10.1002/lom3.10234>

906 Tsutsumi, E., Matsuno, T., Itoh, S., Zhang, J., Senju, T., Sakai, A., Lee, K., Yanagimoto, D., Yasuda, I., Ogawa, H.,  
 907 Villanoy, C., 2020. Vertical fluxes of nutrients enhanced by strong turbulence and phytoplankton bloom around the  
 908 ocean ridge in the Luzon Strait. *Sci. Rep.* 10, 17879. <https://doi.org/10.1038/s41598-020-74938-5>

909 Tuerena, R.E., Williams, R.G., Mahaffey, C., Vic, C., Green, J.A.M., Naveira-Garabato, A., Forryan, A., Sharples, J., 2019.  
 910 Internal Tides Drive Nutrient Fluxes Into the Deep Chlorophyll Maximum Over Mid-ocean Ridges. *Glob.  
 911 Biogeochem. Cycles* 33, 995–1009. <https://doi.org/10.1029/2019GB006214>

912 Van Gennip, S., Martin, A.P., Srokosz, M.A., Allen, J.T., Pidcock, R., Painter, S.C., Stinchcombe, M.C., 2016. Plankton  
 913 patchiness investigated using simultaneous nitrate and chlorophyll observations. *J. Geophys. Res. Oceans* 121,  
 914 4149–4156. <https://doi.org/10.1002/2016JC011789>

915 Vázquez, A., Flecha, S., Bruno, M., Macías, D., Navarro, G., 2009. Internal waves and short-scale distribution patterns of  
 916 chlorophyll in the Strait of Gibraltar and Alborán Sea. *Geophys. Res. Lett.* 36.

917 Vlasenko, V., Stashchuk, N., Hutter, K., 2005. Baroclinic tides: theoretical modeling and observational evidence. Cambridge  
 918 University Press.

919 Waterhouse, A.F., MacKinnon, J.A., Nash, J.D., Alford, M.H., Kunze, E., Simmons, H.L., Polzin, K.L., St. Laurent, L.C.,  
 920 Sun, O.M., Pinkel, R., 2014. Global patterns of diapycnal mixing from measurements of the turbulent dissipation  
 921 rate. *J. Phys. Oceanogr.* 44, 1854–1872.

922 Zaron, E.D., Capuano, T.A., Koch-Larrouy, A., 2023. Fortnightly variability of Chl a in the Indonesian seas. *Ocean Sci.* 19,

923 43–55.  
924 Zhao, Z., Alford, M.H., Girton, J.B., Rainville, L., Simmons, H.L., 2016. Global observations of open-ocean mode-1 M 2  
925 internal tides. *J. Phys. Oceanogr.* 46, 1657–1684.  
926 Zubkov, M.V., Sleigh, M.A., Burkill, P.H., Leakey, R.J., 2000. Picoplankton community structure on the Atlantic  
927 Meridional Transect: a comparison between seasons. *Prog. Oceanogr.* 45, 369–386.  
928